Energy & Environmental Science

www.rsc.org/ees

Volume 6 | Number 12 | December 2013 | Pages 3389–3794

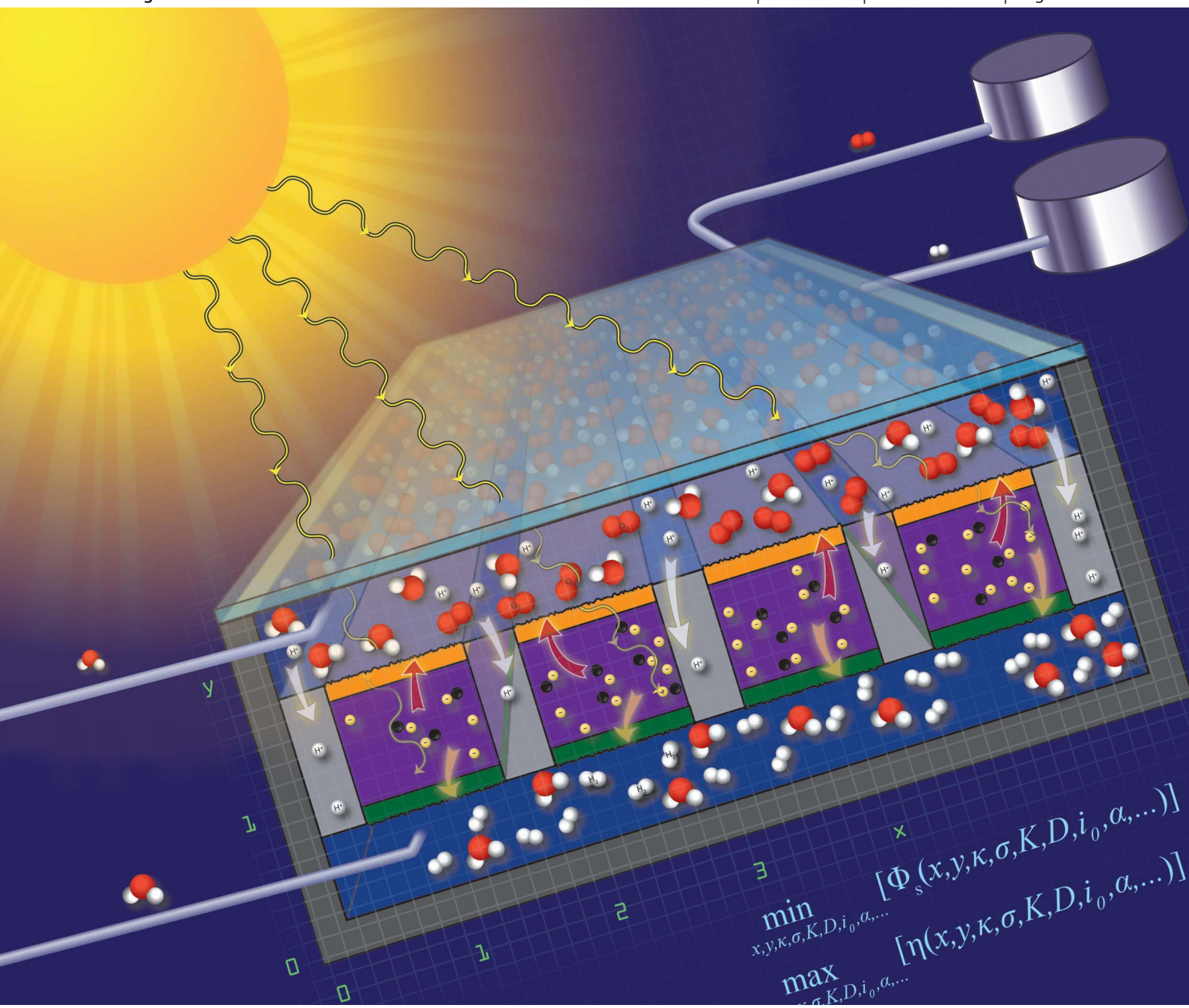

ISSN 1754-5692

RSC Publishing

PAPER

Haussener *et al.*

Simulations of the irradiation and temperature dependence of the efficiency of tandem photoelectrochemical water-splitting systems

1754-5692(2013)6:12;1-Z

Energy & Environmental Science

RSC Publishing

PAPER

View Article Online
View Journal | View Issue

Cite this: *Energy Environ. Sci.*, 2013, **6**, 3605

Simulations of the irradiation and temperature dependence of the efficiency of tandem photoelectrochemical water-splitting systems†

Sophia Haussener,*[ab] Shu Hu,[cd] Chengxiang Xiang,[cd] Adam Z. Weber[b] and Nathan S. Lewis*[cd]

The instantaneous efficiency of an operating photoelectrochemical solar-fuel-generator system is a complicated function of the tradeoffs between the light intensity and temperature-dependence of the photovoltage and photocurrent, as well as the losses associated with factors that include ohmic resistances, concentration overpotentials, kinetic overpotentials, and mass transport. These tradeoffs were evaluated quantitatively using an advanced photoelectrochemical device model comprised of an analytical device physics model for the semiconducting light absorbers in combination with a multi-physics device model that solved for the governing conservation equations in the various other parts of the system. The model was used to evaluate the variation in system efficiency due to hourly and seasonal variations in solar irradiation as well as due to variation in the isothermal system temperature. The system performance characteristics were also evaluated as a function of the band gaps of the dual-absorber tandem component and its properties, as well as the device dimensions and the electrolyte conductivity. The modeling indicated that the system efficiency varied significantly during the day and over a year, exhibiting local minima at midday and a global minimum at midyear when the solar irradiation is most intense. These variations can be reduced by a favorable choice of the system dimensions, by a reduction in the electrolyte ohmic resistances, and/or by utilization of very active electrocatalysts for the fuel-producing reactions. An increase in the system temperature decreased the annual average efficiency and led to less rapid ramp-up and ramp-down phases of the system, but reduced midday and midyear instantaneous efficiency variations. Careful choice of the system dimensions resulted in minimal change in the system efficiency in response to degradation in the quality of the light absorbing materials. The daily and annually averaged mass of hydrogen production for the optimized integrated system compared favorably to the daily and annually averaged mass of hydrogen that was produced by an optimized stand-alone tandem photovoltaic array connected electrically to a stand-alone electrolyzer system. The model can be used to predict the performance of the system, to optimize the design of solar-driven water splitting devices, and to guide the development of components of the devices as well as of the system as a whole.

Received 17th April 2013
Accepted 17th June 2013

DOI: 10.1039/c3ee41302k

www.rsc.org/ees

Broader context

The direct, photoelectrochemical conversion of solar energy and water as well as potentially CO_2 into a storable, high energy density fuel is an interesting option for constructing a renewable energy system. The process mimics functionally plant photosynthesis and is often referred to as artificial photosynthesis. Essential requirements for the feasibility of the process on a large scale and consequently, its impact on our fuel economy, are the sustainable, efficient, stable, and economic implementation *via* solar reactors and their assembly into practical systems. The realization of such systems is challenging because the reactors require the integration of suitable light absorbers, charge generators, and electrocatalysts, which need to be embedded in or connected to conducting phases, while ensuring product separation. The instantaneous efficiency of an operating photoelectrochemical solar-fuel-generator system is a complicated function of the tradeoffs between the light intensity and temperature-dependence of the photovoltage and photocurrent, as well as the losses associated with factors that include ohmic resistances, concentration overpotentials, kinetic overpotentials, and mass transport. This work uses and extends a multi-physics numerical model to estimate the irradiation- and temperature-dependence of the performance of photoelectrochemical devices and to estimate the influence of system design and component characteristics on the overall performance.

[a]*Institute of Mechanical Engineering, École Polytechnique Fédérale de Lausanne, 1015 Lausanne, Switzerland. E-mail: sophia.haussener@epfl.ch*

[b]*Joint Center for Artificial Photosynthesis, Lawrence Berkeley National Laboratory, Berkeley, CA 94720, USA*

[c]*Joint Center for Artificial Photosynthesis, California Institute of Technology, Pasadena, CA 91125, USA. E-mail: nslewis@caltech.edu*

[d]*Division of Chemistry and Chemical Engineering, California Institute of Technology, Pasadena, CA, 91125, USA*

† Electronic supplementary information (ESI) available. See DOI: 10.1039/c3ee41302k

1 Introduction

An operational solar-driven electrochemical-fuel-generating reactor that electrolyzes water or that reduces CO_2 involves light absorbers, charge generators, and electrocatalytic components embedded in or connected to conducting phases, while ensuring product separation for efficiency and safety purposes. All of these components are closely coupled, and their individual performance greatly influences the performance of the integrated generator as a system.[1–4] A comprehensive model that includes the detailed device architecture and accounts for the spatially resolved governing physics is therefore required to evaluate quantitatively the overall efficiency of such a system as a function of the dimensions, component properties, and external variables such as the operating temperature and incident light intensity. Equivalent circuit models have been developed to assess the influence of the properties of different components, such as the choice of light absorber combinations or electrocatalysts, on the overall system performance.[5–8] Recently, models that solve for the governing coupled conservation equations have been developed in 1D,[9] 2D,[10] and 3D,[11] allowing for a better understanding of the interactions between the properties of the components and the design choices of the system. Except for the 2-D model, these models do not account for the detailed characteristics of the solar absorbers, and to date, the models have not been used to examine the performance of the system in response to variations in operational conditions such as variations in the irradiation, changes in temperature, or the use of concentrated solar irradiation.

In this work, the previous modeling and simulation studies of two general types of photoelectrochemical (PEC) reactor designs have been expanded to facilitate a detailed evaluation of the solar-to-fuel system efficiencies as well as the sensitivity of such efficiencies to the system operating conditions and component properties. The instantaneous efficiency of an operating photoelectrochemical system is a complicated function of the trade-offs between various processes including the light intensity and temperature dependence of the photovoltage and photocurrent, as well as the losses associated with ohmic and mass-transport resistances and with concentration and kinetic overpotentials. An advanced PEC device model was therefore developed comprising an analytical model for the semiconducting light absorbers in combination with a spatially resolved multi-physics device model that solved for the governing conservation equations in the various other parts of the system. The model was used to evaluate the variations in the system efficiency due to hourly and seasonal variations in solar irradiation as well as due to changes in the isothermal operating temperature of the system. The system performance characteristics have also been evaluated as a function of the band gaps and quality of the dual-absorber tandem components of the system, the electrolyte conductivity, the device dimensions, and the amount of concentration of the incoming solar irradiation.

2 Theoretical

2.1 Governing equations

2.1.1 Multi-physics model and boundary conditions. The engineering multi-physics PEC model has been described previously.[10] The model solves for charge transport and conservation in the liquid electrolyte phase as well as in the solid conducting phases, *i.e.* the semiconductor, catalyst, and/or transparent conducting oxide (TCO), if present. The electrochemical reactions were assumed to be the electrolysis of water in an acidic environment *via* the anodic oxygen-evolution reaction (OER), eqn (1), and the cathodic hydrogen-evolution reaction (HER), eqn (2).

$$2H_2O \rightarrow O_2 + 4H^+ + 4e^- \quad (1)$$

$$4H^+ + 4e^- \rightarrow 2H_2 \quad (2)$$

The kinetics of the electrochemical water-splitting reaction were modeled by use of Butler–Volmer expressions for the OER and HER, respectively.[12] Species transport was given by an advection/diffusion equation, whereas transport for charged species was given by the Nernst–Planck equation.[12,13] The mass and momentum conservation equations were solved to calculate the pressure and velocity vector fields.[14,15] The model also incorporated recent extensions that provide a more complete description of the semiconductor parts of the system, including specifically the detailed balance limit,[16] and semi-empirical adaptations thereof. The system was assumed to operate at isothermal conditions.

The boundary condition for the light-absorber tandem cell was given by the solar irradiation, *i.e.* by the intensity and spectral distribution of the incident photon flux. The boundary conditions for the current conservation equations were given by the performance of the dual-absorber tandem cell, with the cathode-side electrode assumed to be grounded. Two different boundary conditions for species conservation were used to replicate worst- and best-case product-crossover scenarios. In species boundary condition 1, saturation concentrations of O_2 and H_2 were assumed in the anolyte and catholyte chambers, respectively, and zero concentration of O_2 and H_2 was assumed in the catholyte and anolyte chambers, respectively. These species boundary conditions led to the largest concentration gradient through the separator and consequently led to the largest diffusive fluxes, which in turn resulted in the smallest product collection efficiency. These boundary conditions are appropriate for a flowing system that is continuously provided with a desaturated electrolyte, and thus represent a worst-case scenario. In contrast, in species boundary condition 2, both chambers were assumed to be saturated with H_2 and O_2, respectively, and the electrocatalysts were assumed to not be active in the recombination reaction, thereby representing the situation for a flowing system continuously provided with a saturated, recycled electrolyte. This situation therefore represented the best-case scenario, because no concentration gradient was present and consequently this system provided the largest product collection efficiency.

The permeability of the polymeric separators was assumed to be sufficiently low to withstand the pressure differentials expected in the system during operation; hence convective flows were neglected. A detailed analysis of the influence of convention on the product collection efficiency, as well as the mesh and iteration convergence, along with studies of the proposed model, geometries and boundary conditions, have been described previously.[10] Matlab[17] was used to calculate the characteristics of the dual-absorber tandem cell, with the output of the Matlab code coupled to a commercial finite-element solver, Comsol Multiphysics,[18] to solve the coupled conservation equations with the previously described boundary conditions.

2.1.2 Semiconductor physics. The detailed balance limit[16] describes the amount of incident solar irradiation that is absorbed and produces an electron–hole pair, *i.e.* charge or current, in the semiconductor, minus the current lost due to radiative recombination:

$$i = i_{\mathrm{ph}} - i_{\mathrm{rr}} = q\int_0^{\lambda_g} n_{\mathrm{ph,sol}}(\mathrm{x},\lambda)\mathrm{d}\lambda - q\int_0^{\lambda_g} n_{\mathrm{ph,b}}(\lambda, T)\mathrm{d}\lambda \quad (3)$$

In eqn (3), i_{ph} describes the photocurrent density, i_{rr} is the current density lost due to radiative recombination, λ_g is the optical wavelength corresponding to the band-gap energy of the semiconducting light absorber, $n_{\mathrm{ph,sol}}$ is the spectral photon flux arriving at the surface of the earth at a specific location **x**, and $n_{\mathrm{ph,b}}$ is the spectral photon flux due to blackbody radiation at a temperature T. In the case of a dual-absorber tandem cell, the irradiation is partially absorbed by the top cell and the remaining above-band-gap radiation, $\lambda > \lambda_{\mathrm{g,top}}$, can be absorbed by the bottom cell. A dual-absorber tandem cell was evaluated because such a structure can provide a sufficient potential difference to drive the electrochemical reaction, since the system can produce an open-circuit potential difference that is greater than the equilibrium potential difference for production of H_2 and O_2 from water under standard conditions (1.23 V).

The resulting performance curve of the dual cell can be approximated by a fitted diode equation of the form

$$i = i_{\mathrm{ph}} - i_0\left[\exp\left(\frac{qV + qiR_{\mathrm{ser}}}{kT}\right) - 1\right] - \frac{V}{R_{\mathrm{sh}}}, \quad (4)$$

where i_0 describes the dark saturation current density and R_{ser} and R_{sh} are area-normalized series and shunt resistances ($\Omega\ \mathrm{m}^2$), respectively, and account for resistive losses through the emitter and base, and for contact resistances and current shunting. For the detailed balance limit, the quantity R_{ser} is zero and R_{sh} goes to infinity. Non-zero values of R_{ser} were additionally used in this study to account semi-empirically for the losses within the semiconductor material related to short minority-carrier diffusion lengths and rapid recombination rates. The resulting i–V performance of the light absorbers is characterized by the short-circuit current density, i_{sc}, the open-circuit voltage, V_{oc}, and the fill factor, FF,

$$\mathrm{FF} = \frac{iV|_{\max\{iV\}}}{i_{\mathrm{sc}}V_{\mathrm{oc}}}. \quad (5)$$

2.2 Definitions

The instantaneous solar-to-hydrogen (STH) efficiency of a PEC device is defined as

$$\eta = \frac{iU_\theta}{I}\eta_{\mathrm{F}}\eta_{\mathrm{pc}}, \quad (6)$$

where i is the current density of the operating device, U_θ is the equilibrium potential of the electrochemical reaction under the specified conditions, assumed to be 1.23 V, I is the solar irradiation ($\mathrm{W\ m^{-2}}$) at a specific location, date and time, integrated over a 1.5 Air Mass (AM) spectral distribution, η_{F} is the Faradaic efficiency of the electrode reaction, and η_{pc} is the product collection efficiency. $\eta_{@I=1\ \mathrm{kW\ m^{-2}}}$ describes the instantaneous efficiency for $I = 1\ \mathrm{kW\ m^{-2}}$. The STH definition of eqn (6) is in accord with that described previously,[19,20] although the product collection efficiency is usually assumed to be 1. In our work, parasitic reactions at the electrode were neglected, so that $\eta_{\mathrm{F}} = 1$. The product collection efficiency is defined as

$$\eta_{\mathrm{pc}} = \frac{\int_{A_{\mathrm{a/c}}} i\mathrm{d}A - \int_{A_{\mathrm{sep}}} nFN_{\mathrm{fuel}}\mathrm{d}A}{\int_{A_{\mathrm{a/c}}} i\mathrm{d}A}, \quad (7)$$

i.e. the integrated current over the electrode surface (a: anode or c: cathode) used for the electrochemical reaction minus the product lost due to crossover by diffusion or convection through the chamber–separator surface to the other side of the system, where the species recombines or is lost due to impractical separation issues. The O_2 that crossed over to the catholyte was assumed to constitute an impurity in the fuel stream, which could be purified *via* additional processes such as pressure-swing adsorption. The species boundary condition 2 led to $\eta_{\mathrm{pc}} = 1$, independent of the system design and component dimensions.

The efficiency varies during daytime due to variation in the solar irradiation. The daytime average efficiency is defined by:

$$\overline{\eta}_{\mathrm{d}} = \frac{1}{t_{\mathrm{sunset}} - t_{\mathrm{sunrise}}}\sum_{t=t_{\mathrm{sunrise}}}^{t_{\mathrm{sunset}}}\eta. \quad (8)$$

Similarly, the annual daytime average efficiency was approximated by calculating the average of $\bar{\eta}_{\mathrm{d}}$ over the four characteristic seasonal days:

$$\overline{\eta}_{\mathrm{a}} = \frac{1}{n_{\mathrm{season}}}\sum_{s=1}^{n_{\mathrm{season}}}\overline{\eta}_{\mathrm{d}}. \quad (9)$$

The standard deviation of the annual daytime average efficiency was calculated by:

$$\sigma_{\mathrm{a}} = \sqrt{\frac{1}{n_{\mathrm{season}}(t_{\mathrm{sunset}} - t_{\mathrm{sunrise}}) - 1}\sum_{s=1}^{n_{\mathrm{season}}}\sum_{t_{\mathrm{sunrise}}}^{t_{\mathrm{sunset}}}(\eta - \overline{\eta}_{\mathrm{a}})^2}. \quad (10)$$

2.3 Model parameters

Table S1† summarizes the temperature-dependent reference-case material properties of the various components, *i.e.* the electrolyte,[21] the separator,[22,23] electrocatalysts,[24–30] the conducting layer,[31] solar absorbers,[32–34] *etc.* of the system.

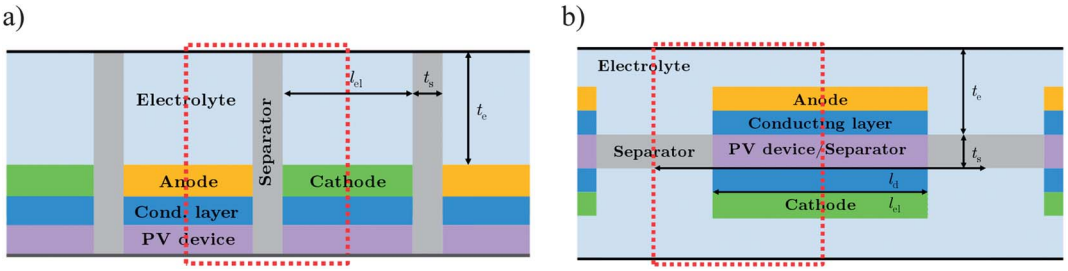

Fig. 1 Schematic of (a) the side-by-side design (Design A), and (b) the top-to-bottom design (Design B) used as model devices, indicating the various dimensional variables, *i.e.* the electrode length, separator thickness, electrolyte height, and device length. The red dotted boxes indicate the modeled unit cells.

2.3.1 Intermittency and local variability of solar irradiation. To evaluate the variation in the performance of the solar-fuel-generator system as a function of the solar-radiation intensity, a particularly well-suited location, Barstow in Southern California, was chosen for investigation. Barstow has a high solar irradiation (yearly average of almost 7 kW h per m^2 per day) and is currently used as a location for large-scale concentrated-solar and photovoltaic power generation. Other comparable irradiation locations are in the Saharan region, central Australia or southern Europe (see Fig. S1a†). Fig. S1b† depicts the solar irradiation (with hourly resolution) of Barstow for a typical meteorological spring, summer, autumn and winter day, respectively, obtained from NREL's TMY3 datasets. NREL's 1.5 AM data were used for the spectral radiation distribution, and these spectral data were scaled according to the solar irradiation using the relationship $I = \int_0^\infty n_{\mathrm{ph,sol}}(\mathrm{x}, \lambda)\mathrm{d}\lambda$.

2.4 Device design

The same basic solar-fuel-generator device designs as in our previous study were investigated herein,[10] therefore representing a continuation of our efforts to model general, but characteristic, device designs. These designs are depicted in Fig. 1, with the red dotted box representing the modeled unit cell.

Design A consists of two light absorbers or (photo)electrodes assembled side-by-side, each immersed in an electrolyte-filled channel but separated from each other by an impermeable, ion-conducting separator and electrically connected *via* an ohmic contact across the bottom of the structure. The two light absorbers or (photo)electrodes could either be a photoanode and a photocathode, or a dual-absorber tandem cell and a catalyst-covered counter-electrode, or a catalyst-covered dual-junction photovoltaic cell and a catalyst-covered counter-electrode. A conductive layer was added on top of the absorber, photovoltaic device, or electrode, to properly model the conducting light absorber or conducting catalyst layer, or a transparent conductive oxide (TCO) layer protecting against the acidic or alkaline environment. As shown previously,[10] this layer can significantly reduce the losses in the system, due to redistribution of the charge closer to the separator, and thus was used as a standard in this study.

Design B consists of one planar dual-absorber tandem cell or catalyst-covered dual-junction photovoltaic cell. This device was also modeled with a conducting layer at the interface between the light absorber and electrocatalysts. The tandem cell was surrounded by an impermeable ion-conducting separator.

For all designs, no potential loss was assumed in the conductive connection for electron transport between the two electrodes. Each design was characterized by an electrode length (l_{el}), a chamber or electrolyte height of thickness t_{e}, and a separator of thickness t_{s}, with Design B additionally characterized by a ratio of the electrode length to the device length ($f = l_{\mathrm{el}}/l_{\mathrm{d}}$). Unless stated otherwise, $t_{\mathrm{s}} = 10$ μm and $f = 0.9$ were used in the calculations. A detailed investigation of the system performance in response to changes in t_{s} and f has been described previously.[10]

3 Results

The detailed balance limit for modeling the performance of a dual-absorber tandem cell was used in the first part of the results. This limit neglects reflection losses and absorption losses due to insufficient optical thickness, and does not account for any charge recombination in the bulk or at the surface of the dual-absorber tandem cell. The detailed balance limit leads to fill factors (FF) of approximately 0.89. Results for a Si/GaAs system (with band gaps of 1.12 eV and 1.43 eV, respectively), which is not a current-matched dual-absorber tandem cell, but which has well-known temperature-dependent material properties, are discussed first. The results are then expanded to arbitrary combinations of dual light absorbers.

3.1 Dual-absorber tandem cell combination – Si/GaAs

Because the temperature dependence of the band gap varies from material to material and is often unknown, a combination of two well-studied materials, Si and GaAs, was used for the first set of investigations. This system facilitated a direct comparison of the performance of a realistic dual-absorber tandem cell-based integrated system under a variety of operating conditions, *i.e.* under varying solar irradiation and at differing isothermal system temperatures.

3.1.1 Daily and annual variations in efficiency. Fig. 2 depicts the model results for the hourly variation in instantaneous efficiency for Design A and Design B, respectively, for four characteristic days during the year. These models used two characteristic combinations of dimensions as well as $\eta_{\mathrm{F}} = 1$,

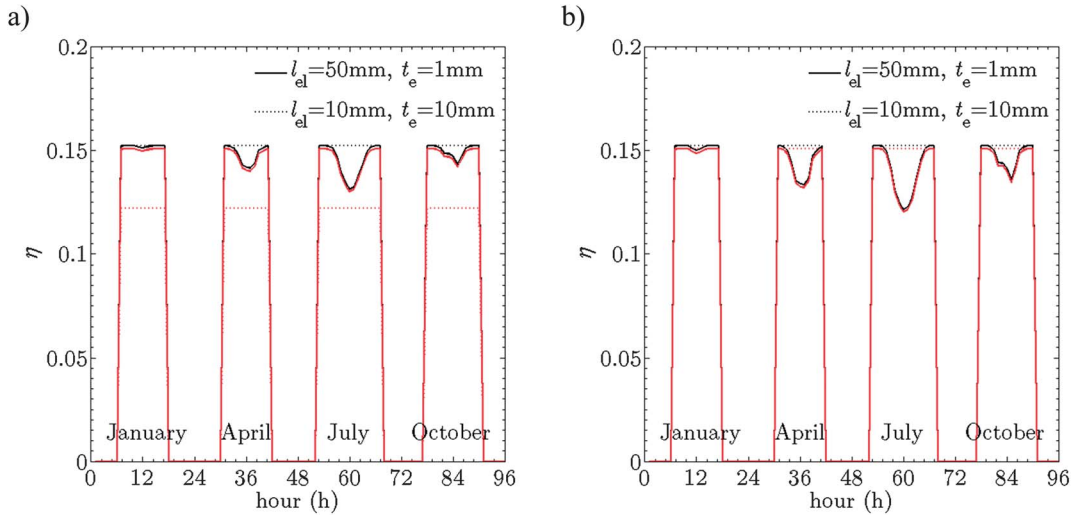

Fig. 2 Efficiency variations of the device during four typical seasonal days for a realistic dual-absorber tandem cell, *i.e.* Si/GaAs multi-junction, for (a) Design A and (b) Design B for two combinations of device dimensions, with assumed $\eta_{pc} = 1$ (black lines), and with η_{pc} calculated according to the species conservation equations (red lines).

with η_{pc} calculated according to the governing species conservation equation. Almost no change in instantaneous efficiency either hourly or for various days in a year was observed when the selected system dimensions resulted in small ohmic electrolyte losses, *i.e.* at small l_{el} and large t_e values.

For optimized versions of Designs A and B (*e.g.* with $l_{el} = 10$ mm and $t_e = 10$ mm), $\bar{\eta}_d$ and $\bar{\eta}_a$ were both 15.3%. In contrast, for $\eta_{pc} = 1$ (species boundary condition 2), as the electrolyte ohmic drop increased (*i.e.* due to larger l_{el} and/or smaller t_e), the variations in efficiency during the day became significant (*e.g.* $l_{el} = 50$ mm and $t_e = 1$ mm yielded 16% and 14% relative efficiency decrease for Designs A and B, respectively). The instantaneous efficiency was lowest during the hours of the day that had the highest solar irradiation. Similarly, the lowest $\bar{\eta}_d$ were observed for the days that had the largest solar irradiation. For $l_{el} = 50$ mm and $t_e = 1$ mm, $\bar{\eta}_a$ was 14.9% for Design A and 14.6% for Design B, with $\bar{\eta}_d = 15.2, 14.8, 14.6, 15.0\%$ for Design A and $\bar{\eta}_d = 15.2, 14.5, 14.1, 14.8\%$ for Design B for a typical winter, spring, summer and autumn day, respectively. When η_{pc} was calculated according to species boundary condition 1 (*i.e.* the worst-case scenario), the values of η, $\bar{\eta}_d$, and $\bar{\eta}_a$ only decreased slightly for Design B ($\eta_{pc} = 0.99$), but η, $\bar{\eta}_d$, and $\bar{\eta}_a$ changed significantly for Design A, especially for geometries having small values of l_{el} ($\eta_{pc} = 0.8$ for $l_{el} = 10$ mm, and $\eta_{pc} = 0.99$ for $l_{el} = 50$ mm).

3.1.2 Effects of system operating temperature. A variation in the isothermal system temperature is expected to produce two competing changes in the system performance characteristics: a

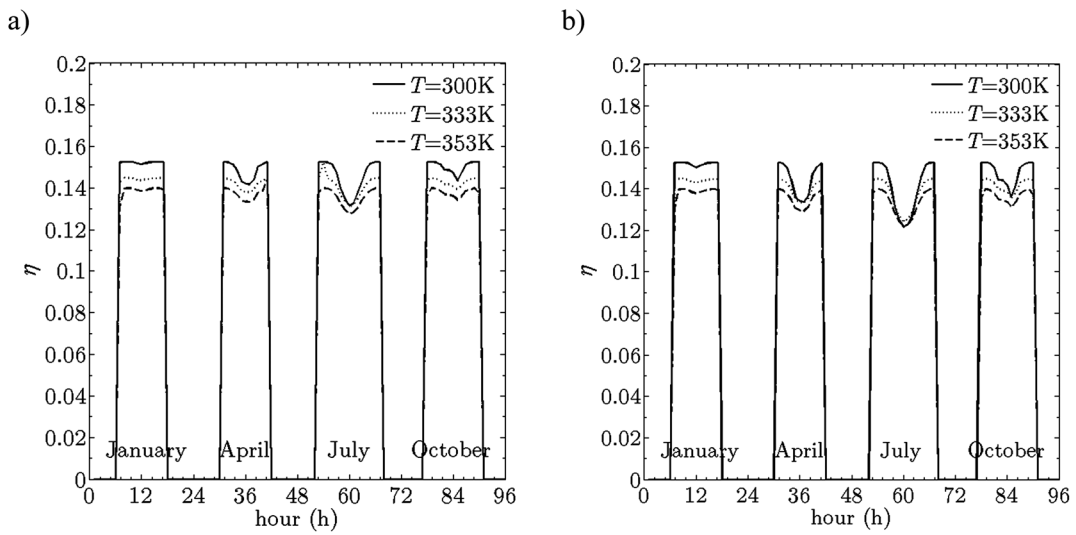

Fig. 3 Efficiency of a PEC device for four typical seasonal days at three isothermal conditions ($T = 300, 333, 353$ K), for the Si/GaAs dual-absorber tandem cells for Designs A and B with $l_{el} = 50$ mm, $t_e = 1$ mm, and $\eta_{pc} = 1$.

reduction in the absorber efficiency due to increased radiation losses, and an enhancement in the transport and kinetics, leading to less efficiency losses associated with these features of the system. The modeling results demonstrated that the specific integrated solar fuel generator system evaluated exhibited a net decrease in maximal efficiency with increasing temperature, due to the reduction in photovoltage with increasing temperature more than offsetting the reduction in losses produced by the increased electrode kinetics and increased electrolyte conductivity at higher temperatures. For example, for $l_{el} = 50$ mm, $t_e = 1$ mm, and $\eta_{pc} = 1$, when the temperature increased from 300 to 353 K, $\bar{\eta}_a$ decreased from 14.6% to 13.6% for Design B (from 14.9% to 13.7% for Design A) and σ_a decreased from 0.90% to 0.49% (0.56% to 0.35% for Design A), see Fig. 3. When the temperature was increased, the efficiency variations during a given day decreased, but the system exhibited lower efficiencies at the beginning and end of each day, *i.e.* exhibited less steep (*i.e.* less rapid) ramp-up and ramp-down phases in response to sunrise or sunset, respectively.

3.1.3 Integrated system *versus* conventional photovoltaic module/electrolyzer system. η, $\bar{\eta}_d$, $\bar{\eta}_a$, σ_a, and the yearly amount of fuel produced by an integrated solar fuel generator system were compared to the behavior of a system instead comprised of a conventional photovoltaic (PV) module-based stand-alone system coupled electrically to a stand-alone electrolysis unit.

The efficiency of the system comprised of the discrete components can be described as

$$\eta_{PV/electrolyzer} = \eta_{PV}\eta_{DC–DC\text{-}converter}\eta_{electrolyzer}, \quad (11)$$

where η_{PV} is the energy-conversion efficiency of the PV-based system, $\eta_{DC–DC\text{-}converter}$ is the efficiency of a DC–DC-converter, and $\eta_{electrolyzer}$ is the efficiency of the electrolyzer, measured by dividing the electrical energy input into the electrolyzer into the value of the free energy of the H_2(g) produced by the electrolyzer. An electrolyzer efficiency of 75% and a DC–DC-converter efficiency of 85% were used in the calculations.

Fig. 4 shows the performance of the stand-alone PV system in combination with the stand-alone electrolyzer system. The dual-absorber tandem cell of the PV system was also taken to consist of Si/GaAs, which does not represent the maximum achievable efficiency of a tandem-cell PV but was chosen to facilitate a straightforward comparison between the performances of the two different types of solar-fuel generation system concepts. Unlike the integrated solar fuel generator system, the stand-alone PV plus stand-alone electrolyzer system displayed its highest η during mid-day and its highest $\bar{\eta}_d$ at mid-year. Increases in the temperature from 300 K to 353 K of the light absorber components of the discrete system decreased $\bar{\eta}_a$ of the stand-alone system combination from 13.3% to 10.6%, with a slight increase in σ_a (from 0.53% to 0.57%). The decrease in $\bar{\eta}_a$ with increasing T was the result of a decrease in V_{oc} with increasing T ($dV_{oc}/dT = 3$ mV K^{-1} and $dFF/dT = 3.2 \times 10^{-4}$ K^{-1} at $I = 1$ kW m^{-2}). Additionally, as depicted in Fig. S4,† the decrease in band gaps at higher T reduced the current matching between the cells, resulting in a decrease in i_{sc} ($di_{sc}/dT = 0.019$ mA cm^{-2} K^{-1} at $I = 1$ kW m^{-2}). Fig. 4c shows the individually normalized, annually integrated fuel production for the stand-alone PV and stand-alone electrolyzer combination, as well as for two cases of the integrated solar fuel generator system: (i) with $l_{el} = 50$ mm and $t_e = 1$ mm and a large total overpotential, and (ii) the optimized case for $l_{el} = 10$ mm and $t_e = 10$ mm with a small, non-limiting total overpotential. The mass of H_2 produced annually, m_{tot,H_2,T_0}, was 7.5, 7.9, and 8.6 kg per m^2 per year for the stand-alone PV and stand-alone electrolyzer combination, integrated system, and optimized integrated system, respectively, at an absorber operating temperature of 300 K in all cases. Hence for these designs, a stand-alone PV and stand-alone electrolyzer combination system would require 13% more area for the production of the same mass of hydrogen per year compared to an integrated system with small total overpotential at $T = 300$ K. At higher temperatures, the stand-alone system combination exhibited a larger decrease in H_2(g) production than did the integrated system, requiring 23% more area for the same production of hydrogen per year as an optimized integrated system, when the light absorbing parts of both systems were operated at $T = 353$ K (and the remainder of the integrated system was maintained at the same temperature as the light absorbers).

3.1.4 Efficiency calculated based on experimentally measured single absorber cells. The measured performance data for single-absorber cells made of GaAs and Si, respectively, as detailed in Table S2,† were used to assess the performance of systems constructed using more realistic, currently available, single solar-absorber cells. Fig. S7† shows the changes in instantaneous efficiency throughout four typical days during the year for such systems. The reduction in V_{oc} for the more realistic, measured absorber system leads to a significant decrease in the performance of a non-optimized integrated system, *i.e.* an integrated system with large overpotentials. The integrated system only outperformed the stand-alone PV system coupled electrically to a stand-alone electrolysis unit when the integrated system was designed to have a significantly reduced overpotential, *i.e.* by use of a decreased electrode length and increased electrolyte height. The annually produced hydrogen mass decreased from 7.5, 7.9, and 8.6 kg per m^2 per year to 6.5, 5.9, 8.3 kg per m^2 per year for the stand-alone PV and stand-alone electrolyzer system, the integrated system, and the optimized integrated system, respectively, when using dual-absorber tandem cells that exhibited realistic, measured performance instead of operating at the ideal, detailed-balance performance limits, at $T = 300$ K. Increases in the isothermal system temperature led to reduced hydrogen production for all systems. Nevertheless, the larger reduction in V_{oc} with increased temperatures for the realistic, measured dual-absorber tandem cell resulted in a larger reduction in annual hydrogen production for the integrated systems compared to the performance of the stand-alone PV and stand-alone electrolyzer system, with increased $d(m_{tot,H_2,T}/m_{tot,H_2,T_0})/dT$ at larger temperatures.

3.2 Arbitrary dual-absorber tandem cell combinations

The system efficiency was also evaluated for arbitrary combinations of absorber materials used over various irradiation

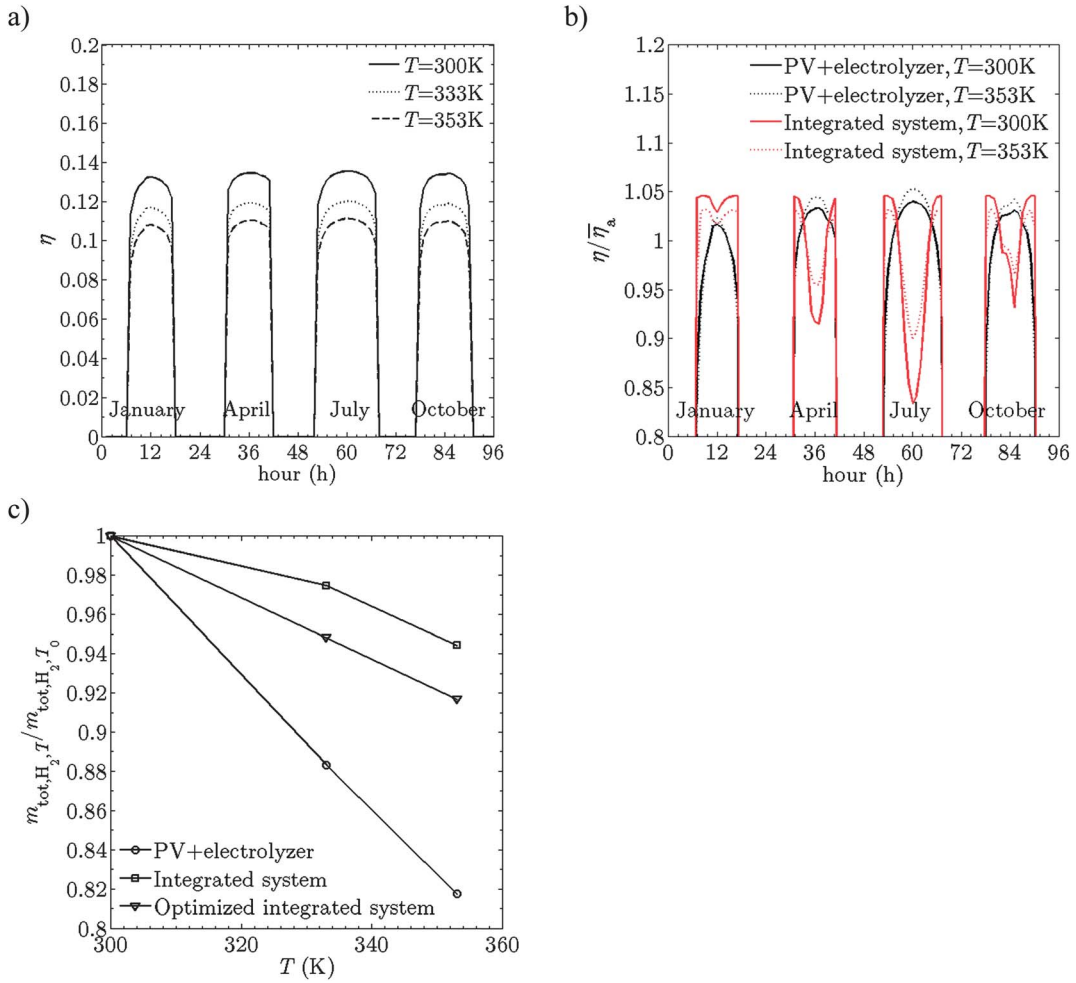

Fig. 4 (a) η of a conventional stand-alone PV system with a Si/GaAs dual-absorber tandem cell, electrically connected to a stand-alone electrolyzer, for four typical seasonal days under three isothermal conditions (T = 300, 333, 353 K), (b) the instantaneous efficiency normalized by $\bar{\eta}_a$ for the stand-alone PV plus stand-alone electrolyzer system compared to the instantaneous efficiency of an integrated solar fuel generator system with l_{el} = 50 mm, t_e = 1 mm, and η_{pc} = 1, and (c) the normalized annually integrated fuel production for the conventional system and for the integrated system (for a system with a large total overpotential as well as for an optimized integrated system with non-limiting total overpotential) with m_{tot,H_2,T_0} = 7.5, 7.9, and 8.6 kg per m^2 per year for the PV + electrolyzer, integrated system, and optimized integrated system, respectively.

conditions, as well as for a variety of isothermal operating temperatures and component dimensions. This procedure allowed evaluation of the effect of variations in the band-gap combinations of the dual-absorber tandem cell on the reactor performance. To minimize the computational effort, the band gaps were varied in ΔE_g = 0.2 eV steps. The temperature-dependent results are shown for the band gaps at the specified isothermal operating temperature. Only results for Design B are depicted, because the difference between the two designs arose mainly from slightly smaller electrolyte ohmic losses in a comparably sized Design A relative to Design B (for species boundary condition 2). A quantitative evaluation of the differences between the dimensionally dependent electrolyte ohmic losses for Designs A and B has been described previously.[10] Of course, η_{pc} is highly dependent on l_{el} in Design A for species boundary condition 1, while η_{pc} is constant for varying l_{el} for Design B, having a value of 0.99 for t_s = 10 μm and l_{el}/l_d = 0.9.

3.2.1 Hourly and seasonal variations in efficiency. For various combinations of dual-absorber band gaps, η and $\bar{\eta}_a$ exhibited a maximum value that was dependent on the design, dimensions, electrolytes, and catalysts used, *i.e.* the electrolyte ohmic losses and the overpotentials of the electrocatalysts. As the total overpotential increased, *i.e.* as the electrolyte ohmic losses and/or reaction overpotentials increased, the maximal efficiency decreased, and the top and bottom band gaps that were required to produce maximal efficiency both increased. For example, Fig. 5 depicts $\eta_{@I=1\ kW\ m^{-2}}$ and $\bar{\eta}_a$ for η_{pc} = 1, for Design B with l_{el} = 10 mm and t_e = 10 mm. This combination of conditions and system design produced a maximum $\eta_{@I=1\ kW\ m^{-2}} = \bar{\eta}_a$ = 31% at 0.8 eV/1.6 eV band gaps (which was the same combination and efficiency values for Design A with l_{el} = 10 mm and t_e = 10 mm). For this optimized design, because the efficiency stays constant as the irradiation level decreases, the instantaneous efficiency values will be essentially

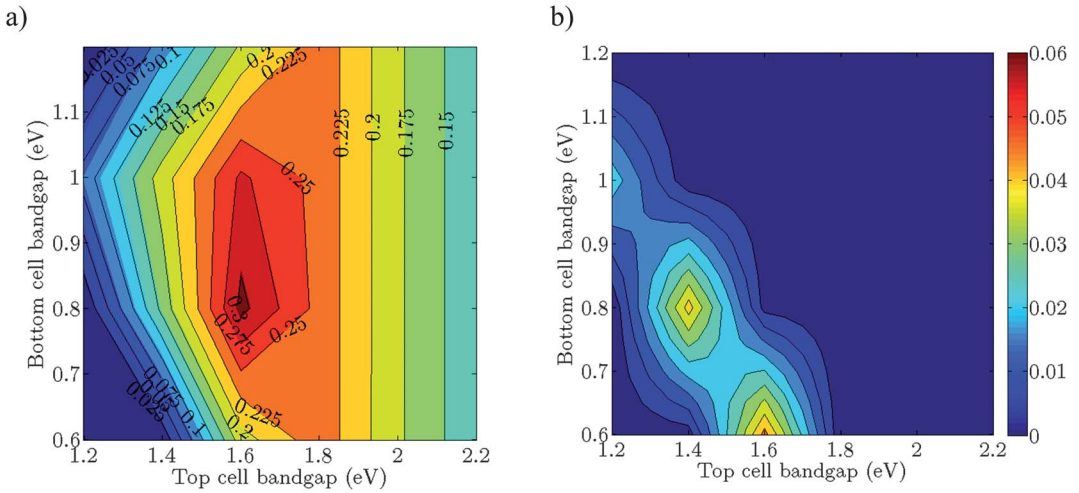

Fig. 5 (a) $\eta_{@I=1\ \mathrm{kW\ m^{-2}}}$ (black lines) and $\bar{\eta}_a$ (color lines), and (b) σ_a, as a function of the band gap of the bottom and top cells of the dual-absorber tandem cell for $T = 300$ K for $l_{el} = t_e = 1$ cm and $\eta_{pc} = 1$.

identical to the annual daytime averaged efficiency values. The value of σ_a was larger for a particular set of band-gap combinations, *i.e.* top cell band-gap plus bottom cell band-gap combinations that showed V_{oc} larger than ~1.55 V (see Fig. S6†) or equal to ~2.2 eV. The value of $\eta_{@I=1\ \mathrm{kW\ m^{-2}}}$ was slightly higher than $\bar{\eta}_a$ for the particular band-gap combinations evaluated.

The performance of the integrated system was compared to that of a stand-alone PV plus stand-alone electrolyzer system ($\eta_{DC-DC\text{-}converter} = 0.85$, $\eta_{electrolyzer} = 0.75$), with both systems having their optimal tandem band-gap combinations at room temperature, *i.e.* 0.8/1.6 eV for the integrated system and 1.0/1.6 eV for the PV plus stand-alone electrolyzer system, respectively. $\bar{\eta}_a$ values were 30.8% and 24.2% for the integrated and the stand-alone PV/electrolyzer systems, respectively. Accordingly, the annually produced hydrogen mass was $m_{tot,H_2,T_0} = 17.4$ kg per m^2 per year for the integrated system as compared to 14.0 kg per m^2 per year for the stand-alone PV–electrolyzer system.

3.2.2 Temperature effects. Fig. 6 depicts $\eta_{@I=1\ \mathrm{kW\ m^{-2}}}$ and $\bar{\eta}_a$ for various band-gap combinations at $T = 353$ K for Design B with $l_{el} = 10$ mm, $t_e = 10$ mm and $\eta_{pc} = 1$. This combination of conditions and system design produced a maximum $\eta_{@I=1\ \mathrm{kW\ m^{-2}}} = \bar{\eta}_a = 29\%$ at 0.8 eV/1.6 eV band gaps (which was the same combination and efficiency values obtained for Design A with $l_{el} = 10$ mm and $t_e = 10$ mm). As was the case for operation at a lower temperature, the peak $\eta_{@I=1\ \mathrm{kW\ m^{-2}}}$ and $\bar{\eta}_a$ efficiencies decreased with increasing reactor electrolyte ohmic losses or electrocatalytic overpotentials. σ_a increased with increasing temperature (Fig. 5b *vs.* 6b).

The performance of the integrated system was compared to that of a stand-alone PV plus stand-alone electrolyzer system ($\eta_{DC-DC\text{-}converter} = 0.85$, $\eta_{electrolyzer} = 0.75$), assuming the same band-gap combination at $T = 353$ K as previously for $T = 300$ K, *i.e.* 0.8/1.6 eV for the integrated system and 1.0/1.6 eV for the stand-alone PV–electrolyzer system, respectively. Fig. S8†

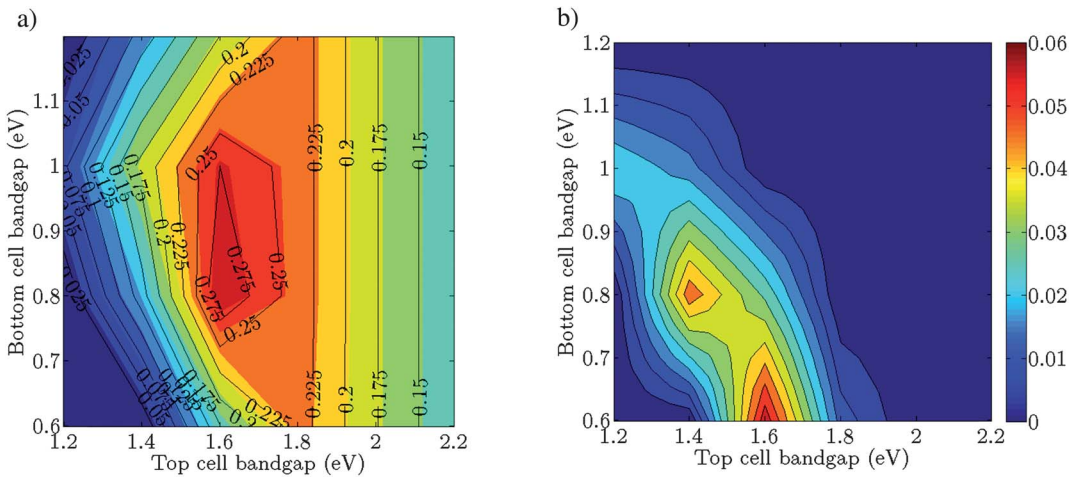

Fig. 6 (a) $\eta_{@I=1\ \mathrm{kW\ m^{-2}}}$ (black lines) and $\bar{\eta}_a$ (color lines), and (b) σ_a, as a function of the band gap of the bottom and top cells of the dual-absorber tandem cell for $T = 353$ K for $l_{el} = t_e = 1$ cm and $\eta_{pc} = 1$.

presents the detailed performance calculations of the optimized stand-alone PV/electrolyzer system and of the optimized integrated system as a function of temperature. $\bar{\eta}_a$ values at 353 K were 29.4% and 21.9% for the integrated and the stand-alone PV–electrolyzer systems, respectively. The annually produced hydrogen mass at 353 K was $m_{tot,H_2,T_0} = 17.0$ and 12.7 kg per m^2 per year for the integrated system and for the stand-alone PV–electrolyzer system, respectively. The band gap of a light absorber usually decreases by 0.002 to 0.006 eV K^{-1} (ref. 34) and, consequently, a straightforward comparison of the temperature-dependent efficiencies of the integrated *versus* stand-alone systems requires a detailed knowledge of the temperature behavior of the band gap, which was not accounted for in evaluating the temperature dependence of these optimal tandem structures because the exact compositions and properties of the light absorbing materials were not specifically known.

3.2.3 Decreasing fill factors. Realistic dual-absorbers do not generally exhibit photovoltages at the detailed balance limit, but additionally exhibit losses such as reflection losses or non-radiative recombination in the bulk as well as at the surfaces of the semiconducting light absorbers. In the modeling, the series resistance in eqn (4) was used to adjust the macroscopic behavior of the tandem cell, *i.e.* the fill factor (FF), between the value appropriate for the detailed balance limit (approximately 0.9) and a value of 0.3 (corresponding to $R_{ser} = 0$ and 0.0533 Ω cm^2, respectively).

For evaluation purposes, the band-gap combination of 1.0 and 1.6 eV was used because it exhibited one of the largest instantaneous efficiencies at 300 K of any system evaluated (Fig. 5). Fig. S5† presents the *i–V*-characteristics for this band-gap combination for various values of the FF, and Fig. 7 depicts the change in $\eta_{@I=1\ kW\ m^{-2}}$ as a function of the FF for various electrode lengths, for Design B with $t_s = 10$ μm and $t_e = 10$ mm, with the dual-absorber structure consisting of materials having 1.0 and 1.6 eV band gaps. The maximal calculated $\eta_{@I=1\ kW\ m^{-2}}$ value was 28%. If a decrease in relative efficiency of 10% were acceptable, dual-absorber tandem cells with FF 0.75 could be used if the geometric design had $l_{el} < 5$ mm.

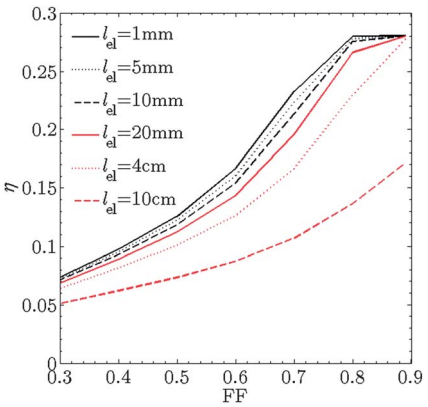

Fig. 7 $\eta_{@I=1\ kW\ m^{-2}}$ as a function of the fill factor of the dual-absorber tandem cell and the electrode length for Design B for $t_e = 10$ mm, and 1.0 and 1.6 eV band-gap combinations for $\eta_{pc} = 1$.

3.2.4 Design impacts. The results obtained in prior modeling efforts have revealed a strong interplay between the performance of the system and the component characteristics, operating conditions, and system design and dimensions. To isolate some general design guidelines for the design dimensions, Fig. 8 presents $\eta_{@I=1\ kW\ m^{-2}}$ for a 1.0 and 1.6 eV band-gap combination dual-absorber tandem cell as a function of the design dimensions l_{el} and t_e. The value of σ_a increased by three orders of magnitude, from 0.003% to 4%, when l_{el} increased from 1 to 100 mm, for $t_e = 10$ mm. The variation in $\bar{\eta}_a$ was larger than +/−5% for $l_{el} > 60$ mm for $t_e = 10$ mm, as depicted in Fig. 8b.

3.2.5 Electrolyte conductivity. The modeling performed herein was primarily focused on the absorber material choices, the design and dimensions of the system, and the operating conditions, because the effects of the separator properties and catalyst choice on the system performance have been evaluated previously.[7,8,10] The simulation however was used to evaluate the

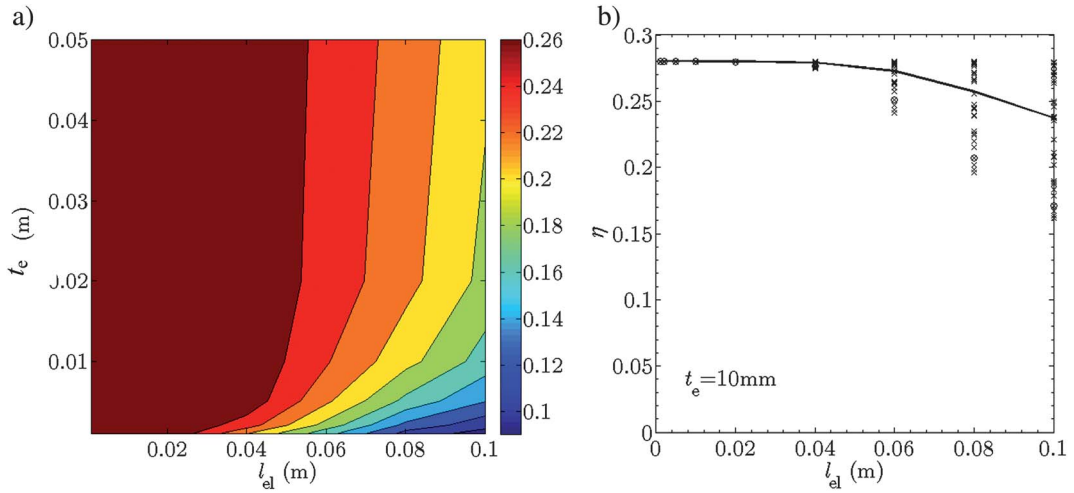

Fig. 8 (a) $\eta_{@I=1\ kW\ m^{-2}}$ as a function of electrode length, l_{el}, and electrolyte height, t_e, and (b) η (crosses) and $\bar{\eta}_a$ (solid line) for $t_e = 10$ mm. Both calculations used top and bottom cell band gaps of 1.0 and 1.6 eV for $\eta_{pc} = 1$. The circled crosses in (b) indicate $\eta_{@I=1\ kW\ m^{-2}}$.

contribution of the electrolyte conductivity to the overall electrolyte ohmic losses as a function of temperature. Accordingly, the conductivity was varied by two orders of magnitude, to approximate a concentration decrease of sulfuric acid from 1.0 M to 0.010 M, corresponding approximately to a pH increase from 0 to 2. This variation in conductivity is also applicable to similar electrolyte concentrations under highly alkaline conditions. Fig. 9 shows $\eta_{@I=1\ \mathrm{kW\ m^{-2}}}$ as a function of electrolyte conductivity, κ_l, for various electrode lengths of Design B with $t_e = 10$ mm and $\eta_{pc} = 1$, with top and bottom cell band gaps of 1.0 and 1.6 eV. Relative to the situation for 1.0 M sulfuric acid, with a conductivity of 40 S m^{-1}, a decrease in relative efficiency of 10% from the maximum efficiency allowed the use of an electrolyte with conductivities of only 0.77 S m^{-1} or 25.97 S m^{-1} if $l_{el} < 1$ mm or $l_{el} < 4$ cm, respectively. Values of $\eta_{@I=1\ \mathrm{kW\ m^{-2}}}$ below 7% were observed when the electrolyte conductivity decreased by two orders of magnitude (from the reference case), even for relatively small electrode lengths.

3.2.6 Concentration of solar radiation. Fig. 10 displays $\eta_{@I=1\ \mathrm{kW\ m^{-2}}}$ of Design B for $t_e = 10$ mm and $\eta_{pc} = 1$, for top and bottom cell band gaps of 1.1 and 1.6 eV under isothermal conditions of $T = 300$ K, as a function of various optical concentration factors, assuming purely direct irradiation. Systems that had a lower total overpotential, *e.g.* that had relatively small electrode lengths, maintained a relatively constant efficiency even at increased optical concentration values. Nevertheless, for optical concentrations of ~100, electrode lengths smaller than 1 mm were required to produce the same efficiencies as those observed under unconcentrated solar irradiation.

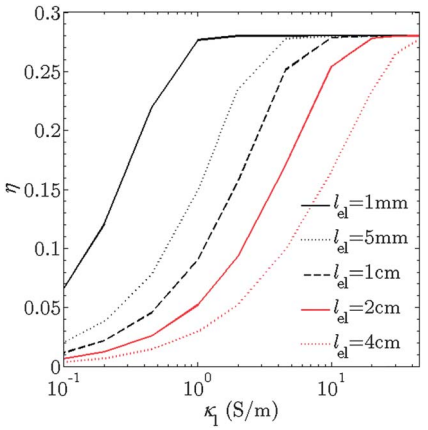

Fig. 9 $\eta_{@I=1\ \mathrm{kW\ m^{-2}}}$ as a function of electrolyte conductivity for various electrode lengths, l_{el}, for $t_e = 10$ mm and $\eta_{pc} = 1$, for top and bottom cell band gaps of 1.0 eV and 1.6 eV.

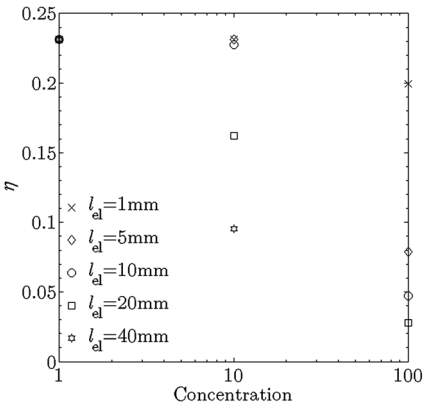

Fig. 10 $\eta_{@I=1\ \mathrm{kW\ m^{-2}}}$ as a function of solar irradiation concentration for various electrode lengths, l_{el}, for $t_e = 10$ mm and $\eta_{pc} = 1$, for top and bottom cell band gaps of 1.1 and 1.6 eV.

4 Discussion

4.1 Hourly and seasonal variations in efficiency

According to eqn (6), the instantaneous efficiency of an integrated system can be maximized if the system is designed such that the total overpotential produces an optimal overlap between the *i–V* performance of the dual-absorber tandem cell (the power curve) as it intersects the load curve in the plateau of the power curve, *i.e.* the reactor runs at or close to the short-circuit current density of the light absorbers. This design requires small ohmic electrolyte potential losses, *i.e.* small reactor dimensions and highly conducting electrolytes, and fast reaction kinetics, *i.e.* electrocatalysts with low overpotentials. Because the short-circuit current density is proportional to the solar irradiation, the instantaneous efficiency during hourly and seasonal variations of solar irradiation can be constant, *i.e.* $\sigma_a = 0$, only if the system is designed such that the dual-absorber tandem-cell *i–V* performance intersects the load curve in the plateau region for the maximal expected irradiation. Otherwise the instantaneous efficiency will vary during the day and year, *i.e.* $\sigma_a \neq 0$, with local minima at midday and global minima in summer, *i.e.* at the largest irradiation conditions during the day or year. This behavior occurs because at the largest irradiation, the system will be driven at the highest current density that, in turn, produces the largest overpotentials for the electrocatalysts and electrolyte ohmic losses. Hence, the intersection between the power and load curve is displaced away from the plateau and lies in the declining region of the power curve of the dual-absorber tandem cell. The variations in instantaneous efficiency during the day or year can be relaxed, or eliminated, by use of designs and components that produce low total overpotentials, *i.e.* low electrolyte ohmic losses *via* small dimensions and more conducting electrolytes or *via* the use of better catalysts, *i.e.* lower reaction overpotentials.

For comparable system dimensions, Design A in general showed larger $\bar{\eta}_d$ and $\bar{\eta}_a$ values than Design B, because the electrolyte ohmic losses are smaller for Design A, due to the orthogonalization between the irradiation direction and the main ionic-flow direction for Design A.[10] Nevertheless, for the worst-case scenarios of η_{pc} (species boundary condition 1), Design A's efficiencies decreased significantly, especially at smaller dimensions that are favorable for electrolyte ohmic losses but unfavorable for crossover processes.

For combinations of solar absorbers with arbitrary band gaps, the band-gap combination of the dual-absorber tandem cell that produced the maximum $\eta_{@I=1\ \mathrm{kW\ m^{-2}}}$ was dependent on the total overpotential of the device. Increases in the total

overpotential of the device resulted in larger band gaps needed to produce maximal $\eta_{@I=1\ kW\ m^{-2}}$ but also resulted in smaller maximum $\eta_{@I=1\ kW\ m^{-2}}$ for that specific band-gap combination than for devices with non-limiting overpotentials. Larger band gaps produced larger V_{oc} values (see Fig. S6†), and consequently provided the required potential to sustain the production of fuels, but at the expense of smaller photocurrent densities, thereby producing smaller maximal $\eta_{@I=1\ kW\ m^{-2}}$. The hourly and seasonal variations in efficiency increased for a particular set of band-gap combinations, and were a function of the total overpotential, *i.e.* the design, dimensions, electrolyte conductivity and electrocatalysts. These band-gap combinations barely produced sufficient photopotential to drive the device; hence for certain irradiation conditions the system operated in the declining region of the dual-absorber tandem-cell *i–V*-performance curve. Additionally, the two local maxima observed in annual efficiency variation can be associated with the band-gap-dependent distribution of i_{sc} and FF (see Fig. S6†).

The passage of clouds over a device can also result in fluctuations that can be as severe as complete ramp down and ramp up. Hence, mitigation mechanisms and analyses similar to those described herein can be applied to assess the variability in efficiency as a result of cloud cover, but are outside the scope of this work. In addition, seasonal temperature variations can also impact the total system efficiency, as discussed below.

4.2 Temperature effects

A change in operating temperature produced two competing effects on the system performance: (i) decreased photoperformance, *i.e.* a smaller short-circuit current density, a smaller open-circuit potential, and a smaller FF, of the dual-absorber tandem cell, and (ii) a decreased electrolyte ohmic drop and electrocatalytic overpotential, due to increased electrolyte–separator conductivity and more rapid interfacial kinetics (larger exchange current densities and smaller Tafel slopes). The maximum modeled efficiency decreased with increasing temperature primarily because the current matching became less optimal due to the decrease in band-gap energy with increasing temperature. Nevertheless, for a device with $\sigma_a \neq 0$, *i.e.* that exhibited large overpotentials, the midday variations in efficiency decreased with increasing system temperature, because the electrolyte ohmic losses and the reaction overpotentials decreased, leading to lower total overpotential and consequently moving the operating point towards the plateau region of the load curve. However, the efficiencies at the beginning and end of the day decreased, *i.e.* less steep ramp-up and ramp-down phases were observed. The lower FF for higher temperatures (see Fig. S4†), which becomes critical for low solar irradiation, accounted for this aspect of the system performance. The latter effect (less steep ramp up/down) increased σ_a with increasing temperature and was the dominant effect for systems with non-limiting total overpotentials, while the former effect (reduced variation during midday) decreases σ_a with increasing temperature and was found to be the dominant effect for systems with large total overpotentials.

These two mutually contradicting effects on the efficiency variation with increasing temperature, increased variation at ramp up/down and decreased variation during midday, imply that an operating device would benefit from the lower temperatures in the morning and the evening, therefore operating at maximum efficiency under such conditions. For a device with large overpotentials, maximal solar irradiation and consequently operating at higher temperatures in the middle of the day would shift the system onto a performance curve that had a lower maximal efficiency but that also exhibited lower midday variability. This behavior likely produces a higher overall efficiency relative to a system with large overpotentials that was constantly operated at low temperatures during the day. For example, relative to a cooled system that was constantly operated at 300 K, the efficiency could be increased by 1% in July simply by dynamically adapting to the temperature during the day. This approach could be performed in synchronicity with an increase in temperature during a day and would reduce the cooling power required to maintain the system under isothermal conditions during the whole day.

4.3 Decreasing fill factors

A series resistance was included in the calculated detailed balance limit to account for a portion of the realistic *i–V* performance of dual-absorber tandem cells, *i.e.* non-ideal absorption of radiation and charge recombination within the bulk and at the surface of the light absorbers. The performance decreased significantly as the FF decreased, because the system was more readily forced further away from operating at i_{sc}, even for very small system dimensions, *i.e.* small total overpotentials (large electrolyte conductivity, electrocatalysts with small overpotential). A small plateau region was observed, namely for the 1.0 and 1.6 eV band-gap combination with small system dimensions ($l_{el} < 1$ cm) or generally small total overpotentials, for which a dual-absorber tandem cell with a FF 0.75 could be used with essentially no accompanying decrease in efficiency. For this band-gap combination, the provided potential was significantly larger than the value required by devices with small total overpotential. Hence, even with smaller FF values, the system still operated in the plateau region of the *i–V* performance of the tandem cell.

4.4 Design impacts

A strong interplay was observed between the properties of the materials, the operational conditions, and the device design and dimensions. The modeled efficiency was relatively insensitive to changes in the height of the electrolyte, especially for small electrode lengths. This result is consistent with the conclusions of our previous study.[10] Electrode lengths smaller than 45 mm and electrolyte heights larger than 5 mm produced equal values of $\eta_{@I=1\ kW\ m^{-2}}$. The simulation also allowed evaluation, for particular dual-absorber band-gap combinations, of the maximal electrode lengths needed to produce negligible σ_a. The larger electrode lengths of the system produced larger values of σ_a. This behavior resulted from larger electrolyte ohmic losses at larger l_{el}; consequently, the device

was more easily driven to operate in the declining region of the *i–V* performance of the dual-absorber tandem cell. This effect was especially pronounced at larger solar irradiations, which produced the largest photocurrent densities and photovoltages.

4.5 Electrolyte conductivity

Despite the design and its dimensions, the electrolyte conductivity nevertheless still contributed significantly to the ohmic electrolyte losses. Consequently, a larger electrolyte conductivity produced more favorable system performance. Large conductivities are usually associated with highly acidic or alkaline environments, or with buffered electrolytes that can lead to additional concentration gradient-dependent potential losses. The modeling described herein focused on operation in highly acidic or alkaline electrolytes, while still allowing for a two order-of-magnitude variation in the electrolyte conductivity. The modeling indicated that for small electrode lengths, the system could tolerate almost a two order-of-magnitude reduction in electrolyte conductivity without a significant reduction in efficiency. Nevertheless, when a critical ohmic electrolyte resistance was reached, the efficiency decreased steeply as the electrolyte conductivity decreased.

4.6 Concentration of solar irradiation

Optical concentration can potentially reduce the cost of some solar energy-conversion systems due to a reduction in the device size and component mass. Nevertheless, with concentrated solar irradiation, the current density increases proportionally and therefore larger overpotentials are produced in the device. For small device total overpotentials, the results indicated that optical concentrations of 10× can be used with essentially no decrease in maximum efficiency of the modeled systems. However, the temperature will likely increase at increased optical concentration, thereby producing either additional efficiency losses, as described above, or requiring an increase in cooling power.

4.7 Integrated system *versus* conventional photovoltaic module–electrolyzer system

The comparison between an optimized tandem integrated PEC device and an optimized stand-alone tandem PV plus stand-alone electrolyzer system (DC–DC-converter efficiency = 0.85, electrolyzer efficiency = 0.75) showed that the integrated system always outperformed the stand-alone PV–electrolyzer system. This behavior was associated with the fact that the integrated system operated at larger "internal electrolyzer" efficiencies due to the low current densities. The better performance of the integrated system relative to the stand-alone PV–electrolyzer system was observed for systems that utilized the same light absorber tandem cell structure (Si/GaAs), *i.e.* $\bar{\eta}_a = 15.3\%$ *versus* 13.3% for the integrated and stand-alone PV–electrolyzer systems, respectively, as well as for individually optimized systems, *i.e.* $\bar{\eta}_a = 30.8\%$ *versus* 24.2% for the band-gap optimized integrated and band-gap optimized stand-alone PV–electrolyzer systems, respectively. Additionally, the decrease in efficiency with increasing temperature was less steep for an integrated system compared to a stand-alone PV–electrolyzer system, because the integrated system benefited from enhanced transport at increased temperatures.

5 Summary and conclusions

The largest variations in efficiency during the day and year were observed at the local or global irradiation maxima. These variations in efficiency were especially pronounced for systems that had a relatively large total overpotential, *i.e.* for devices with a larger electrode length, smaller electrolyte height, lower electrolyte conductivity, and/or smaller band-gap combinations of light absorbers. A system designed to produce constant efficiency throughout the year therefore should be designed to operate at maximum efficiency under the maximal solar irradiation at the planned location.

Increased isothermal device temperatures led to a reduction in maximal device efficiency and less steep ramp up and ramp down at the beginning and end of the day, due to decreased performance of the dual-absorber tandem cell with increased temperature. Nevertheless, the midday and midyear variations in efficiency decreased, due to a reduction in the total overpotential, *i.e.* reduced transport and kinetic losses, with increasing device temperatures. The competition between decreased light absorber performance and increased transport performance with increasing temperature leads to an interesting conclusion, in that a PEC device with a limiting overpotential can gain in annually averaged efficiency if it is not driven at constant lower system temperature but instead is dynamically adapted to higher operating temperatures as the solar irradiation increases, which will occur naturally throughout a day. For a device with low, non-limiting overpotentials, *i.e.* $\sigma_a = 0$, the increased transport performance with increased temperature will not lead to additional gains in efficiency and, consequently, such a device will show the best annual performance at low temperatures.

The model predicts that systems with lower total overpotential, *i.e.* smaller electrode dimensions, electrolytes with higher conductivity, or catalysts with lower overpotentials, could use dual-absorber tandem cells with lower quality, *i.e.* smaller FF, and still operate at maximum efficiency. Nevertheless, the smallest acceptable FF for Design B with an electrode length of 1 mm was still only 0.75 for a reduction in relative efficiency of less than 1%.

For various combinations of dual-absorber tandem cells and device dimensions, the maximal tolerable electrode length for which the system would operate at constant efficiency throughout the year was determined and was translated into a lower limit for the electrolyte conductivity or an upper limit for electrocatalyst overpotential losses that will produce acceptable overall device performance with $\sigma_a = 0$. Variations in the electrolyte conductivity can significantly influence the device performance. The device was tolerant of small electrolyte conductivities provided that the device had small values of other overpotentials, such as those that can be produced by a reduction in the electrode length. The modeling also revealed the limitations in terms of system dimensions for operation

under concentrated solar irradiation, in that for smaller system sizes an optical concentration of at least 10× can be achieved without significant decrease in efficiency.

The modeling also allowed for comparison of integrated systems and conventional stand-alone PV plus stand-alone electrolyzer systems. The simulations showed that integrated systems can benefit from the small current densities by significantly increasing the "internal electrolyzer efficiency". A conventional PV plus electrolyzer system (with electrolyzer efficiency of 75% and DC–DC-converter efficiency of 85%) made from exemplary Si and GaAs tandem light absorbers required 13% more area to produce the same annual amount of hydrogen as would be produced by an integrated system with comparable solar absorbers. Additionally, the discrete component PV plus electrolyzer system did not benefit from enhanced kinetics and transport due to enhanced temperatures, additionally enlarging the performance difference, *i.e.* 23% more area was needed for a discrete component system with the light absorbers at 353 K *versus* an integrated system at an isothermal operating temperature $T = 353$ K. Similarly, the integrated system outperformed the stand-alone PV and stand-alone electrolyzer system even when both systems were operated with individually optimized tandem light absorbing structures, *i.e.* with the best performing band-gap combinations and small dimensions, leading to $\bar{\eta}_a$ values of 30.8% and 24.2% for the integrated and stand-alone PV–electrolyzer systems, respectively, at $T = 300$ K.

The construction of a complete, operational solar fuel generator is of intense current interest and is the focus of numerous experimental programs globally.[35] This work provides a predictive modeling and simulation framework for evaluation of the performance of such systems under varying temperature and irradiation conditions. The multi-physics model allowed for an in-depth understanding and quantification of the influence of device design, dimensions, component characteristics (absorber choice and quality, electrolyte choice and conductivity), and operational conditions (irradiation variation, irradiation concentration, temperature) on device performance. The model can be used to optimize the design and component choice of solar-driven water splitting devices, and to guide the development of components of the devices as well as of the system as a whole.

Nomenclature

Latin symbols

A	Surface area (m^2)
E_g	Band-gap energy (eV)
f	Ratio of the electrode length to the device length, l_{el}/l_d
FF	Form factor
i	Current density (A m^{-2})
i_0	Dark saturation current density (A m^{-2})
I	Solar irradiation (W m^{-2})
n	Number of electrons
n_{ph}	Spectral photon flux (m^{-3} s^{-1})
k	Boltzman constant (J K^{-1})
l	Length (m)
q	Elemental charge (C)
R_{ser}	Area-normalized series resistance (Ω m^{-2})
R_{sh}	Area-normalized shunt resistance (Ω m^{-2})
t	Thickness (m)
T	Temperature (K)
U_θ	Equilibrium potential under standard conditions (V)
V	Potential (V)

Greek symbols

κ_l	Liquid conductivity (S m^{-1})
λ	Wavelength (m)
σ_a	Standard deviation of annual averaged efficiency
η	Efficiency
$\bar{\eta}_d$	Daytime averaged efficiency
$\bar{\eta}_a$	Annual daytime averaged efficiency

Subscripts

a	Anode
b	Black body
c	Cathode
d	Device
el	Electrode
F	Faradaic
g	Gap
oc	Open circuit
pc	Product collection
ph	Photon
rr	Reradiation
s	Separator
sc	Short circuit.

Acknowledgements

We acknowledge the Joint Center for Artificial Photosynthesis, a DOE Energy Innovation Hub, supported through the Office of Science of the U.S. Department of Energy under Award Number DE-SC0004993. We thank Harry Atwater for fruitful discussions on temperature-dependent analysis of realistic systems.

References

1 O. Khaselev and J. A. Turner, *Science*, 1998, **280**, 425–427.
2 S. Y. Reece, J. A. Hamel, K. Sung, T. D. Jarvi, A. J. Esswein, J. J. H. Pijpers and D. G. Nocera, *Science*, 2011, **334**, 645–648.
3 J. Brillet, J.-H. Yum, M. Cornuz, T. Hisatomi, R. Solarska, J. Augustynski, M. Graetzel and K. Sivula, *Nat. Photonics*, 2012, **6**, 824–828.
4 H. Dotan, O. Kfir, E. Sharlin, O. Blank, M. Gross, I. Dumchin, G. Ankonina and A. Rothschild, *Nat. Mater.*, 2013, **12**, 158–164.

5 M. T. Winkler, C. R. Cox, D. G. Nocera and T. Buonassisi, *Proc. Natl. Acad. Sci. U. S. A.*, 2013, **110**, E1076–E1082.
6 R. Rocheleau and E. Miller, *Int. J. Hydrogen Energy*, 1997, **22**, 771–782.
7 Y. Surendranath, D. K. Bediako and D. G. Nocera, *Proc. Natl. Acad. Sci. U. S. A.*, 2012, 1–5.
8 S. Hu, C. Xiang, S. Haussener, A. D. Berger and N. S. Lewis, An analysis of the optimal band gaps of light absorbers in integrated tandem photoelectrochemical water-splitting systems, *Energy Environ. Sci.*, 2013, DOI: 10.1039/C3EE40453F.
9 L. Andrade, T. Lopes, H. A. Ribeiro and A. Mendes, *Int. J. Hydrogen Energy*, 2011, **36**, 175–188.
10 S. Haussener, C. Xiang, J. M. Spurgeon, S. Ardo, N. S. Lewis and A. Z. Weber, *Energy Environ. Sci.*, 2012, **5**, 9922–9935.
11 C. Carver, Z. Ulissi, C. Ong, S. Dennison, G. Kelsall and K. Hellgardt, *Int. J. Hydrogen Energy*, 2012, **37**, 2911–2923.
12 A. J. Bard and L. R. Faulkner, *Electrochemical methods – Fundamentals and applications*, John Wiley & Sons, New York, 2nd edn, 2000.
13 J. Newman and K. Thomas-Alyea, *Electrochemical systems*, John Wiley & Sons, 2004.
14 S. Patankar, *Numerical heat transfer and fluid flow*, McGraw-Hill Inc., USA, 1980.
15 J. H. Ferziger and M. Peric, *Computational methods for fluid dynamics*, Springer-Verlag, 2001.
16 W. Shockley and H. J. Queisser, *J. Appl. Phys.*, 1961, **32**, 510–519.
17 M. 2012b, *Matlab*, 2012.
18 C. 4.3, *Comsol Inc.*, 2012.
19 Z. Chen, T. F. Jaramillo, T. G. Deutsch, A. Kleiman-Shwarsctein, A. J. Forman, N. Gaillard, R. Garland, K. Takanabe, C. Heske, M. Sunkara, E. W. McFarland, K. Domen, E. L. Miller, J. A. Turner and H. N. Dinh, *J. Mater. Res.*, 2010, **25**, 3–16.
20 M. G. Walter, E. L. Warren, J. R. McKone, S. W. Boettcher, Q. Mi, E. A. Santori and N. S. Lewis, *Chem. Rev.*, 2010, **110**, 6446–6473.
21 H. E. Darling, *J. Chem. Eng. Data*, 1964, **9**, 421–426.
22 Y. Sone, P. Ekdunge and D. Simonsson, *J. Electrochem. Soc.*, 1996, **143**, 1254–1259.
23 H. Ito, T. Maeda, A. Nakano and H. Takenaka, *Int. J. Hydrogen Energy*, 2011, **36**, 10527–10540.
24 J. O. M. Bockris, I. A. Ammar and A. K. M. S. Huq, *J. Phys. Chem.*, 1957, **61**, 879–886.
25 G. Lodi, E. Sivieri, A. Battisti and S. Trasatti, *J. Appl. Electrochem.*, 1978, **8**, 135–143.
26 K. Kinoshita, *Electrochemical Oxygen Technology*, John Wiley and Sons, Inc., 1992.
27 L. Kriksunov, L. Bunakova, S. Zabusova and L. Krishtalik, *Electrochim. Acta*, 1994, **39**, 137–142.
28 A. Damjanovic, A. Dey and J. O. Bockris, *J. Electrochem. Soc.*, 1966, **113**, 739–746.
29 N. M. Markovic, B. N. Grgur and P. N. Ross, *J. Phys. Chem. B*, 1997, **101**, 5405–5413.
30 W. Sheng, H. A. Gasteiger and Y. Shao-Horn, *J. Electrochem. Soc.*, 2010, **157**, B1529–B1536.
31 J. George and C. Menon, *Surf. Coat. Technol.*, 2000, **132**, 45–48.
32 Y. Varshni, *Physica*, 1967, **34**, 149–154.
33 R. Pässler, *Phys. Status Solidi B*, 2003, **236**, 710–728.
34 P. Singh and N. Ravindra, *Sol. Energy Mater. Sol. Cells*, 2012, **101**, 36–45.
35 T. A. Faunce, W. Lubitz, A. W. B. Rutherford, D. MacFarlane, G. F. Moore, P. Yang, D. G. Nocera, T. A. Moore, D. H. Gregory, S. Fukuzumi, K. B. Yoon, F. A. Armstrong, M. R. Wasielewski and S. Styring, *Energy Environ. Sci.*, 2013, **6**, 695–698.

Electronic Supplementary Material (ESI) for Energy & Environmental Science

SUPPORTING INFORMATION FOR

Simulations of the irradiation and temperature dependence of the efficiency of tandem photoelectrochemical water-splitting systems

Sophia Haussener, Shu Hu, Chengxiang Xiang, Adam Z. Weber, and Nathan S. Lewis

Spatial and temporal variation in solar irradiation

Figure S1 depicts the spatial, hourly and seasonal variation in solar irradiation.

a) b)

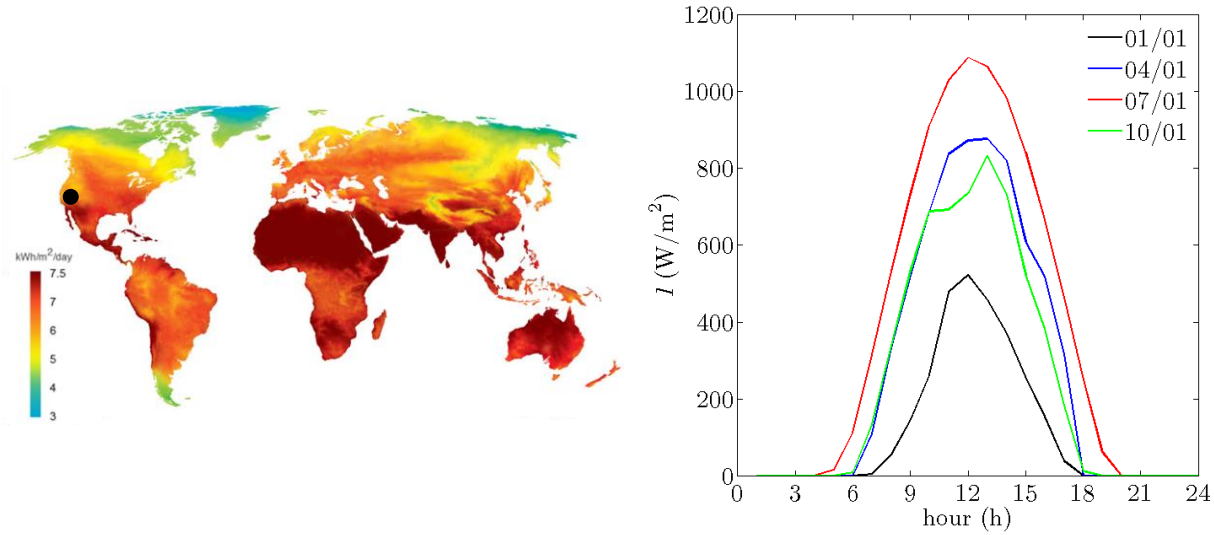

Figure S1. Annual mean of hourly solar irradiation (a), and hourly resolved irradiation for four characteristic seasonal days in Barstow, California (b).

Materials properties

Table S1 presents the properties of the materials chosen for the system as well as their temperature dependence between 300 K and 353 K. The increase in solution conductivity with temperature was approximated by

$$\kappa_{\mathrm{l}} = \kappa_{\mathrm{l},T=293\mathrm{K}}\left(1+\alpha\left[T-293\right]\right), \qquad \text{(S1)}$$

where $\kappa_{l,T=293K}$ and α were fitted to experimental data available for 1 M sulfuric acid [1]. The temperature dependence of the conductivity of a non-permeable polymeric membrane, i.e. Nafion, was given by

$$\kappa_{mem} = \kappa_{0,mem} \exp\left(-\frac{E_a}{RT}\right), \quad \text{(S2)}$$

where E_a represents the activation energy [2]. The decrease in the equilibrium potential for the one-step water-electrolysis reaction with increasing temperature is given by

$$U = U_\theta - T \cdot \alpha_3, \quad \text{(S3)}$$

where U_θ is the equilibrium potential assuming a hydrogen reference electrode, and α_3 is given by the temperature-dependence of the Gibbs free energy (ΔG=-nFU).The electrochemical reactions were described by Butler-Volmer expressions,

$$i_{R,OER/HER} = i_{0,OER/HER}\left[\left(\frac{c_{red}}{c_{red,0}}\right)^{\gamma_{red}} \exp\left(\frac{\alpha_{a,OER/HER} F\eta_{op}}{RT}\right) - \left(\frac{c_{ox}}{c_{ox_0}}\right)^{\gamma_{ox}} \exp\left(\frac{-\alpha_{c,OER/HER} F\eta_{op}}{RT}\right)\right], \quad \text{(S4)}$$

with

$$i_{0,OER/HER} = i_{0,OER/HER,T_{ref}} \exp\left(-\frac{E_a}{RT}\right). \quad \text{(S5)}$$

The kinetic parameters used in the study are for state-of-the-art catalysts, i.e. Pt-based electrodes for the HER reaction and RuO_2-based electrodes for the OER reaction. For the HER, transfer coefficients between 1 and 2 have been reported [3], and values of $\alpha_{a,HER} = \alpha_{c,HER} = 1$ were assumed. For the OER, $\alpha_{a,HER} = 1.7$ and $\alpha_{c,HER} = 0.1$ were used, which is consistent with the reported 35 mV per decade Tafel slope [4] as well as an assumed negligible back reaction at the potential of interest. The temperature dependences were extracted from various experimental studies [5-8].

The temperature-dependent conductivity of a transparent conducting oxide (TCO) layer was given by

$$\sigma_{\mathrm{TCO}} = \frac{A_0}{R_{\mathrm{s},0} t} \exp\left(-\frac{\Delta E}{kT}\right), \tag{S6}$$

where R_s is the sheet resistance of the TCO material of thickness t, and ΔE is the activation energy in eV [9]. The temperature dependence of the band gap was described using the Varshi model[10-12],

$$E_g = E_{g,0} - \frac{\alpha_2 T^2}{T + \beta} \tag{S7}$$

with the constants α_2 and β fitted to experimental data for Si and GaAs [12].

Table S1. Parameters used for the various materials and components in the system, as a function of temperature.

Parameter	Value	Param.	Value	Param.	Value	Ref.
$i_{0,\mathrm{OER},T\mathrm{ref}}$	4.62 A cm^{-2}	$E_{a,\mathrm{OER}}$	48.6 kJ mol^{-1}	-	-	5, 6, 13
$i_{0,\mathrm{HER},T\mathrm{ref}}$	142.02 A cm^{-2}	$E_{a,\mathrm{HER}}$	28.9 kJ mol^{-1}	-	-	7, 8
$\kappa_{0,\mathrm{mem}}$	22.73 S m^{-1}	$E_{a,\mathrm{mem}}$	2 kJ mol^{-1}	-	-	2, 14
$\kappa_{l,T=293\mathrm{K}}$	40 S m^{-1}	α	0.019 K^{-1}	-	-	1
$R_{s,0}$	10 Ω/□	A_0	3.695	ΔE	0.033 eV	9
$E_{g,0,\mathrm{Si}}$	1.1557 eV	$\alpha_{2,\mathrm{Si}}$	7.021·10^{-4} eV K^{-1}	β_{Si}	1108 K	10, 12
$E_{g,0,\mathrm{GaAs}}$	1.5216 eV	$\alpha_{2,\mathrm{GaAs}}$	8.871·10^{-4} eV K^{-1}	β_{GaAs}	572 K	10, 12
A_{H2}	-48.1611	B_{H2}	55.2845	C_{H2}	16.8893	15
A_{O2}	-66.7354	B_{O2}	87.4755	C_{O2}	24.4526	15

Table S1 also presents the set of parameters used in this study. The supporting information shows detailed current-voltage behavior and characteristics (i_{sc}, V_{oc}, FF) of dual-

absorber tandem cells for hourly, seasonal, and local variations in the solar irradiation and for various isothermal system temperatures.

The temperature-dependence of the saturation concentrations of H_2(g) and O_2(g) were given by

$$c_{\mathrm{sat},k} = \exp\left(A_k + B_k / (T/100\mathrm{K}) + C_k \ln(T/100\mathrm{K})\right) / M_{\mathrm{H_2O}} \cdot 1000, \qquad \text{(S8)}$$

in the units mol/m^3.

Semiconductor performance and characterization

Figure S2 depicts the change in current-voltage characteristics of a dual-absorber tandem cell (made of 1.7/1.1 eV bandgap materials) during a typical summer day at Barstow.

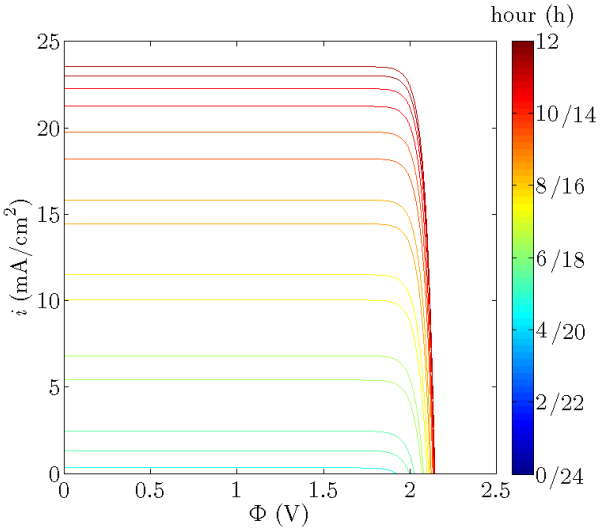

Figure S2. Current vs. voltage performance and its variation during the day of a dual-absorber tandem cell composed of 1.7/1.1 eV bandgap materials for a typical July day.

Figure S3 depicts the short-circuit current density, open-circuit voltage, and fill factor (FF) of two characteristic types of dual-absorber tandem cells, i.e. (*i*) a current-matched cell composed of 1.7/1.1 eV band gap materials (i.e. GaAsP/Si), and (*ii*) a non-current matched

cell composed of 1.43/1.1 eV band gap materials (i.e. GaAs/Si). The short-circuit current density is proportional to the solar irradiation.

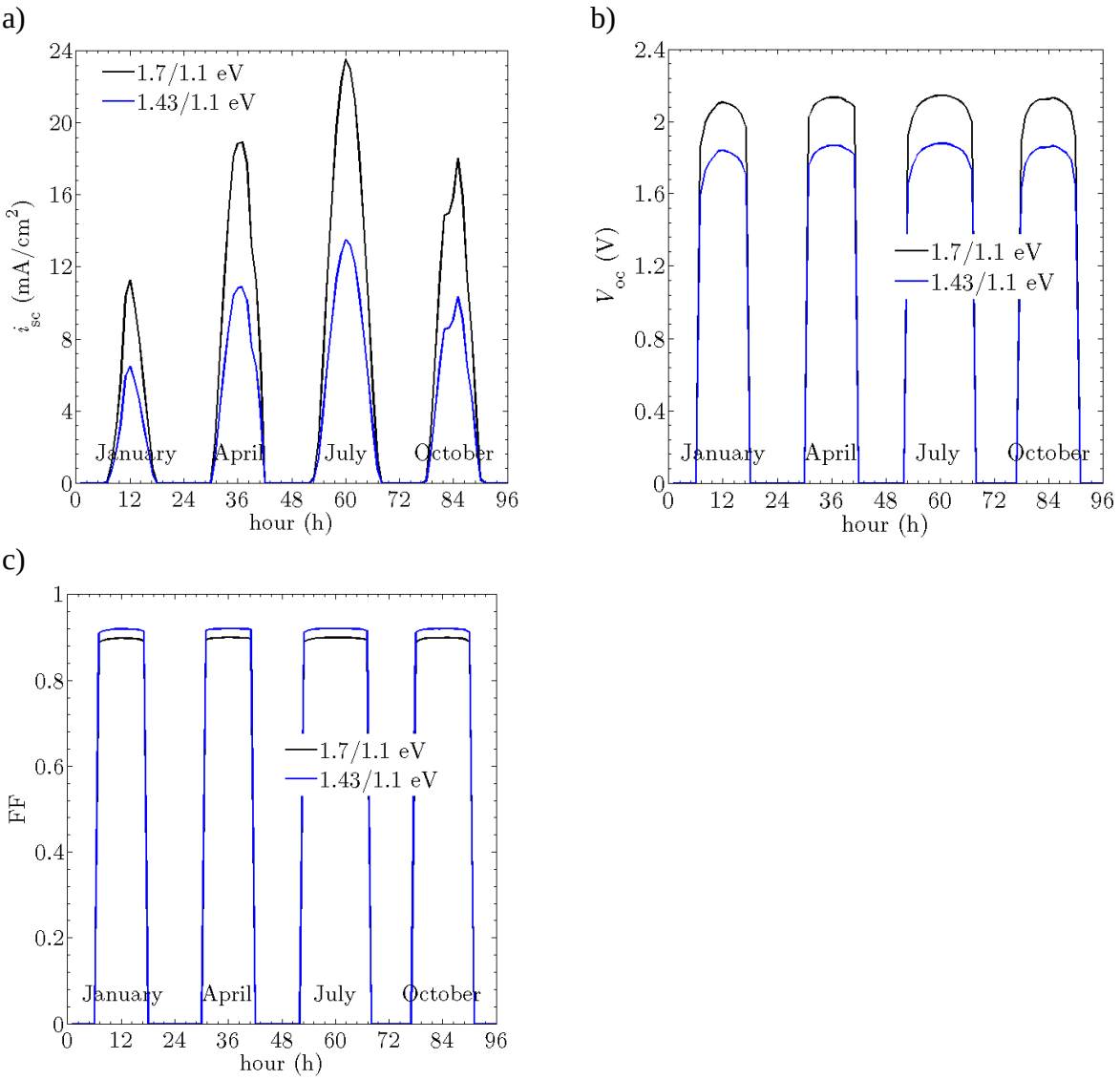

Figure S3. Variation in short-circuit current density (a), open-circuit potential difference (b), and form factor (c), of the current matching (1.7/1.1 eV) and non-current matching (1.43/1.1 eV) dual-cells during four typical days in winter, spring, summer, and fall.

Figure S4 depicts the short-circuit current density, open-circuit voltage, and fill factor (FF) of two dual-absorber tandem cells, for variations in the isothermal system temperature (between 300 K and 353 K). The short-circuit current density decreases for a dual-absorber tandem cell

because the current-matching band gap combination evolves into a less favorable current combination (a non-current matching) as the temperature is changed. The results are in accord with reported data [12].

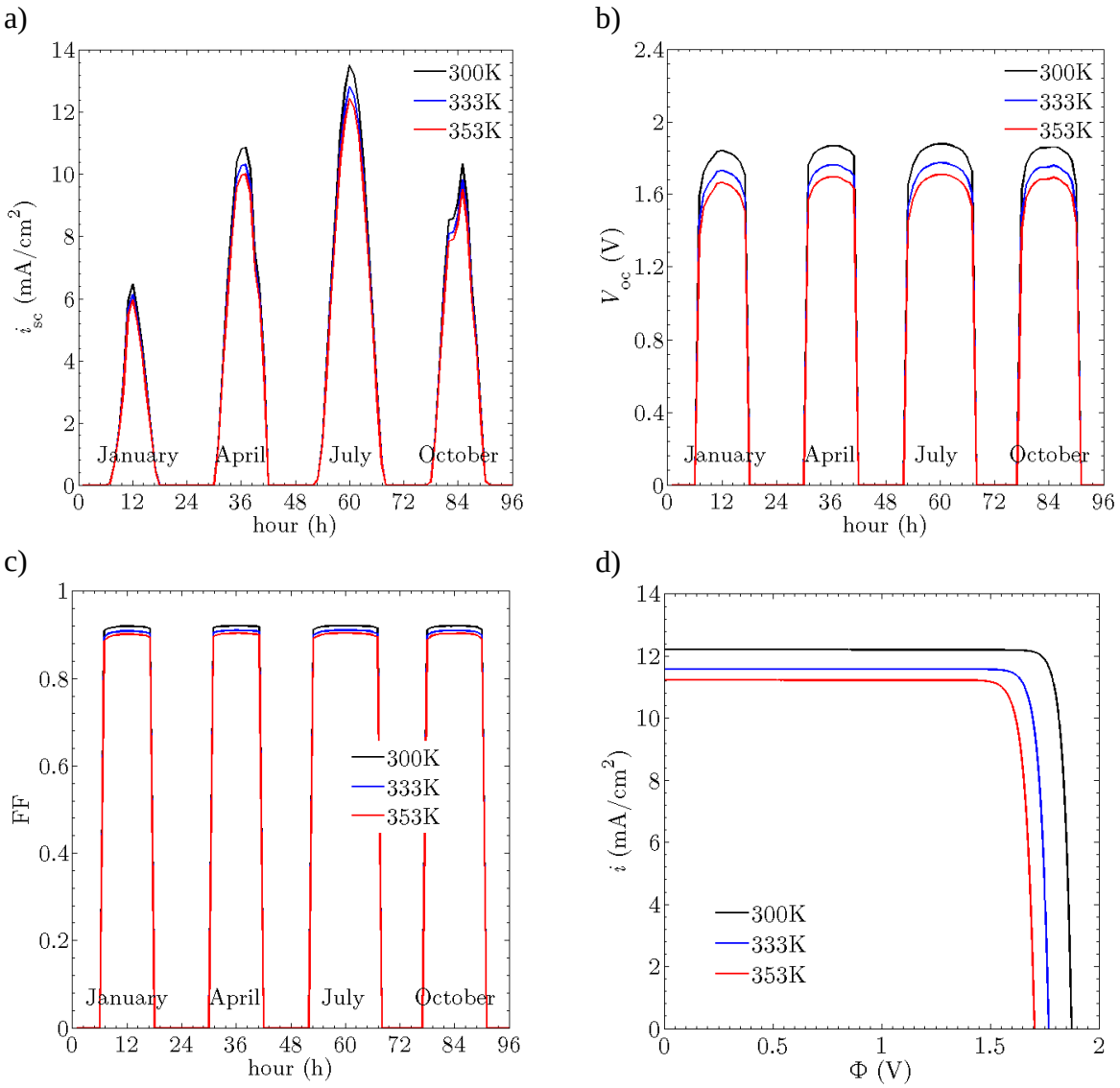

Figure S4. Temperature-dependent short-circuit current density (a), open-circuit voltage (b), fill factor (c), and i-V-performance for I=1kWm^{-2}, for the dual cell composed of 1.43/1.1 eV band gaps (at room temperature).

An artificial series resistance within the semiconductor model was used to more accurately account for non-idealities. Figure S5 depicts the current density vs. voltage performance of a dual-absorber tandem cell.

Figure S6 depicts the changes in short-circuit current density, open-circuit voltage, and fill factor for various combinations of band gaps at 1kW/m^2, 1.5 AM solar irradiation.

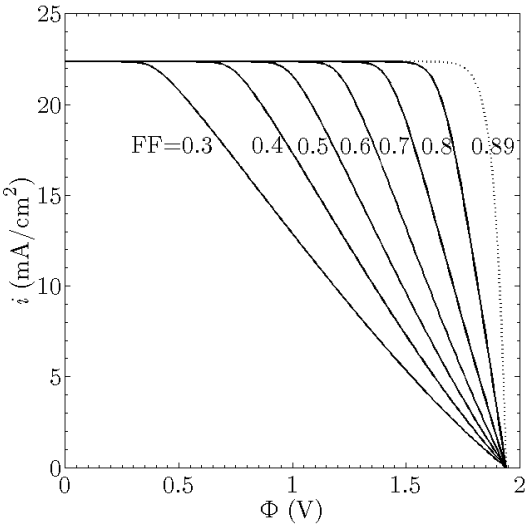

Figure S5. Current density vs. voltage performance and its change with increasing series resistance, i.e. decreasing fill factor, for a 1.6/1.0 eV band gap dual-absorber tandem cell for 1 sun and 1.5 AM solar irradiation. The dotted line depicts the detailed balance limit.

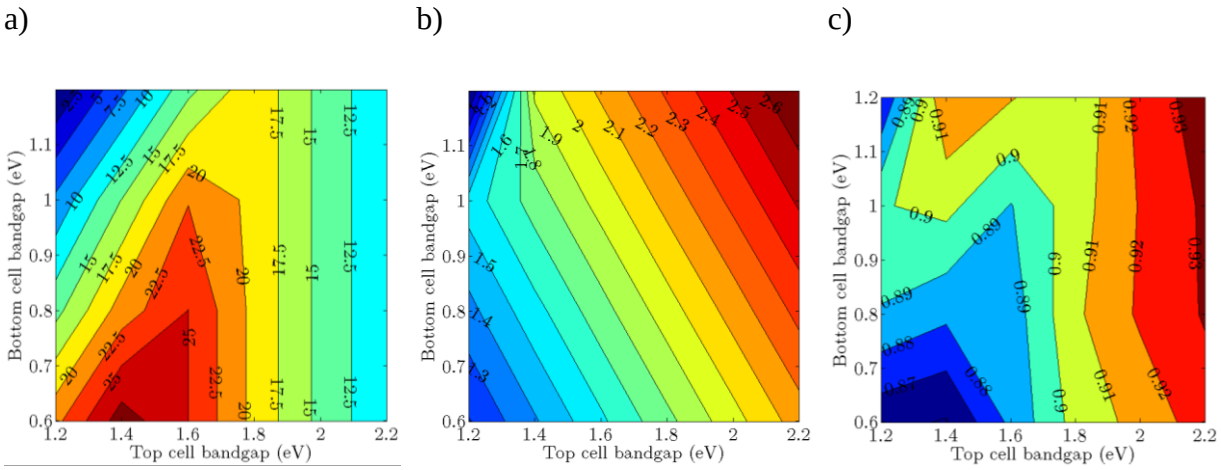

Figure S6. (a) Short-circuit current density (mA/cm^2), (b) open-circuit voltage (V), and (c) fill factor for various combinations of top and bottom bandgap energies at 1 kW/m^2, 1.5 AM solar irradiation.

Realistic dual absorbed tandem cell

The performance of a realistic dual absorber tandem cell composed of currently available Si and GaAs cells has also been predicted via the measured performance of individual single cells, as given in Table S2.

Table S2. Measured short-current density, open-circuit voltage, fill factor, and temperature coefficients of commercial GaAs (Alta devices[*]) or Si (Schott [†,16]) solar cells.

	GaAs cell	Si cell
$i_{sc,0}$	24.39 mA cm^{-2}	42.7 mA cm^{-2}
$V_{oc,0}$	1.09 V	0.706 V
FF	0.842	0.828
α_{abs}	0.084 % K^{-1}	0.03 % K^{-1}
γ_{abs} or β_{abs}	0.187 % K^{-1}	2 mV K^{-1}

The intensity dependence and temperature dependence of the performance can be approximated as:

$$i_{sc} = i_{sc,0}\left(1+\alpha_{abs}\left[T-298\right]\right)\cdot\frac{I}{I_0}, \quad \text{(S9)}$$

$$V_{sc} = V_{sc,0}\left(1+\gamma_{abs}\left[T-298\right]\right), \quad \text{(S10)}$$

$$V_{oc} = V_{oc,0}-\beta_{abs}\left(T-298\right), \quad \text{(S11)}$$

with the measured temperature coefficients α_{abs}, γ_{abs}, and β_{abs}. The performance of the tandem configuration was calculated by using the Si and GaAs cells in series, with the irradiation of the bottom cell (Si) reduced by the fraction of light absorbed by the top cell (GaAs), as given by its temperature-dependent band gap energy calculated using equation (S7).

[*] www.altadevices.com/pdfs/single_cell.pdf
[†] http://www.schott.com/photovoltaic/english/download/schott_perform_mono_255-270_3bb_new_frame_data_sheet_en_0312.pdf

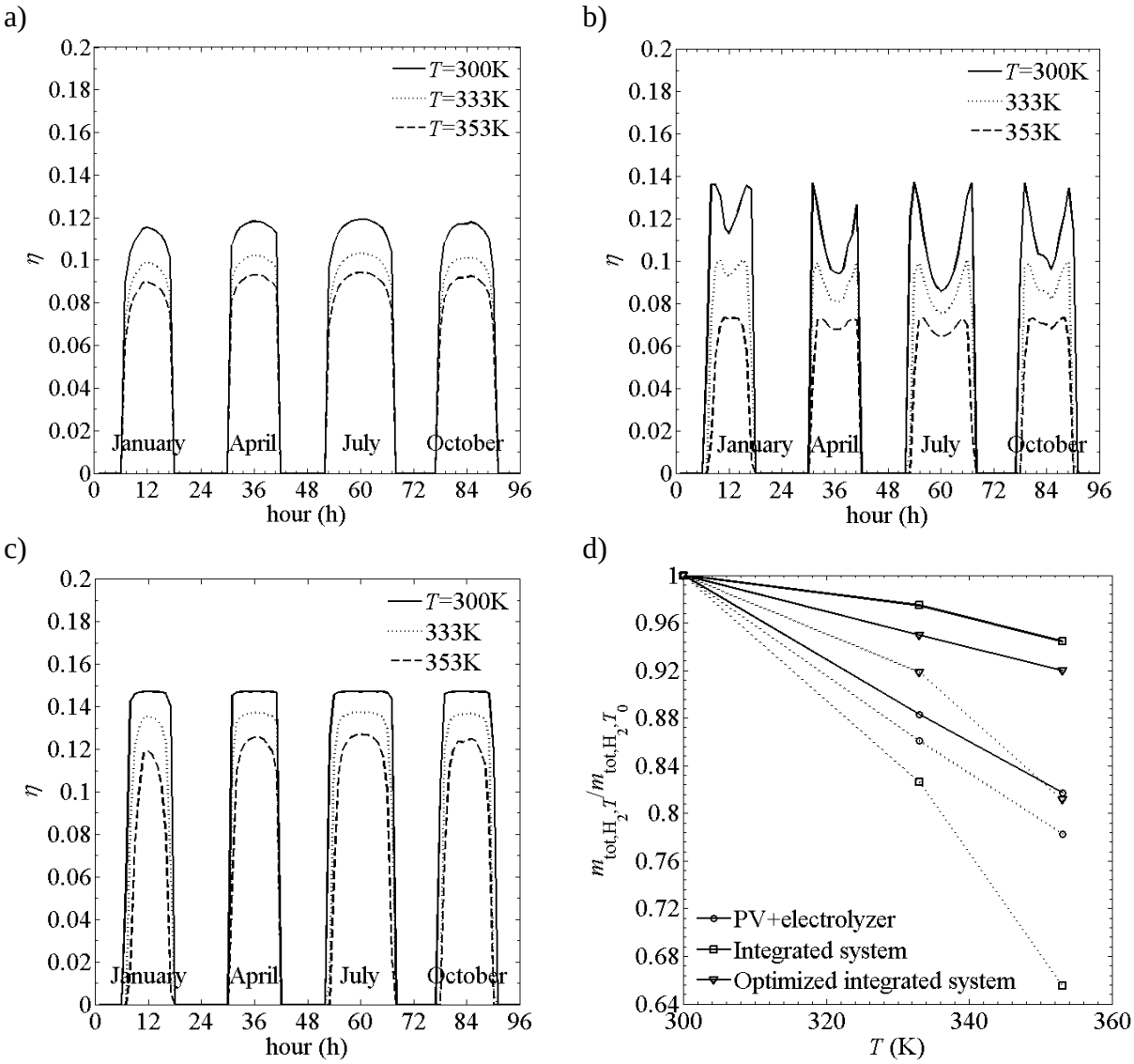

Figure S7. (a) η of a conventional stand-alone PV system with a Si/GaAs dual absorber tandem structure based on the measured individual cell performance, with the tandem cell electrically connected to a stand-alone electrolyzer, for four typical seasonal days at three isothermal conditions (T = 300, 333, 353 K), and (b,c) η of a PEC device with a Si/GaAs dual absorber tandem-cell based on measured individual cell performance for four typical seasonal days at three isothermal conditions (T = 300, 333, 353 K) for design B with η_{pc} = 1, (b) l_{el} = 50 mm, and t_e = 1 mm, and (c) l_{el} = 10 mm, and t_e = 10 mm, and (d) the normalized annually integrated fuel production for the conventional system and for the integrated system with m_{tot,H_2,T_0} = 6.6, 5.9, and 8.3 kg m^{-2} year^{-1} for the PV+electrolyzer, the integrated system, and the optimized integrated system, respectively, for detailed balance limit (solid line) and the realistic case (dotted line).

The resulting performance of the integrated system and a stand-alone tandem PV plus stand-alone electrolyzer system (electrolyzer efficiency of 75% and a DC-DC-converter efficiency of 85%) using Si/GaAs-based dual absorber tandem-cell based on measured single cell performance are depicted in Figure S7.

As observed for systems that were assumed to operate in the Shockley-Quiesser limit, unlike the integrated solar fuels generator system, the realistic stand-alone PV plus stand-alone electrolyzer system displayed its highest η during mid-day and its highest $\overline{\eta}_{d}$ at mid-year. Increases in the temperature from 300 K to 353 K of the light absorber components of the discrete system decreased $\overline{\eta}_{a}$ of the stand-alone system combination from 11.2% to 8.7%, with a slight increase in σ_{a} (from 0.24% to 0.27%). The integrated system for design B with $\eta_{pc} = 1$, $l_{el} = 50$ mm, and $t_{e} = 1$ mm, showed $\overline{\eta}_{a}$ = 11.3% and 6.4% for T = 300 K and 353 K, respectively, with slight increase in σ_{a} (from 0.02% to 0.03%). Changing the dimensions of the system to $l_{el} = 10$ mm, and $t_{e} = 10$ mm resulted in an increase in $\overline{\eta}_{a}$ to values of 14.3% and 10.6% for T = 300 K and 353 K, respectively, with decrease in σ_{a} (from 0.34% to 0.28%). Figure S7d shows the normalized, annually integrated fuel production for the stand-alone PV and stand-alone electrolyzer combination, as well as for two cases of the integrated solar fuels generator system: *i*) with $l_{el} = 50$ mm and $t_{e} = 1$ mm and a large total overpotential, and *ii*) the optimized case for l_{el} = 10 mm and t_{e} = 10 mm with a small, non-limiting total overpotential. The mass of H_2 produced annually, m_{tot,H_2,T_0}, was 6.6, 5.9, and 8.3 kg m^{-2} $year^{-1}$ for the stand-alone PV and stand-alone electrolyzer combination, the integrated system, and the optimized integrated system, respectively at an absorber operating temperature of 300 K in all cases.

Integrated vs. stand-alone PV plus stand-alone electrolyzer system

η, $\overline{\eta}_d$, $\overline{\eta}_a$, σ_a, and the yearly amount of fuel produced by an integrated solar fuels generator system were compared to the behavior of a system instead comprised of a conventional photovoltaic (PV) module-based stand-alone system coupled electrically to a stand-alone electrolysis unit. The efficiency of the system comprised of the discrete components can be described by equation (11). An electrolyzer efficiency of 75% and a DC-DC-converter efficiency of 85% were used in the calculations.

Figure S8 shows the performance of the stand-alone PV system in combination with the stand-alone electrolyzer system. The dual absorber tandem-cell of the PV system was taken to consist of 1.0/1.6 eV band-gaps at all temperatures, which showed to lead to the best tandem-cell PV performance. Unlike the integrated solar fuels generator system, the stand-alone PV plus stand-alone electrolyzer system displayed its highest η during mid-day and its highest $\overline{\eta}_d$ at mid-year. Increases in the temperature, from 300 K to 353 K, of the light absorber components of the discrete system decreased $\overline{\eta}_a$ of the stand-alone system combination from 24.2% to 21.9%, with a slight increase in σ_a (from 0.97% to 1.13%). The band-gap of the light absorber usually decreases by 0.002 to 0.006 eV K^{-1} [12] and therefore this straight-forward comparison neglects the penalty due to reduced current matching, i.e. lower i_{sc}, of such a dual absorber tandem-cell at higher temperatures.

a)

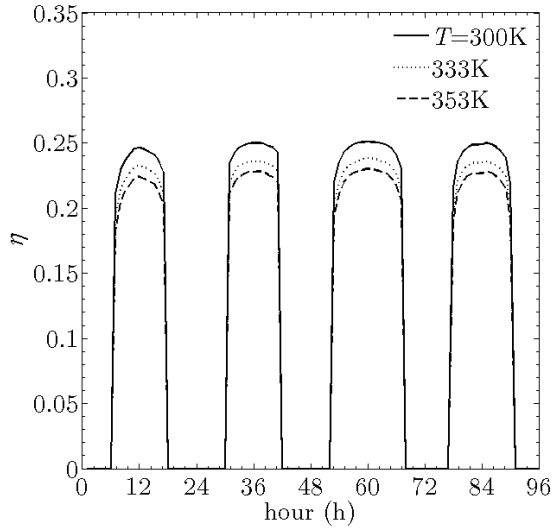

b)

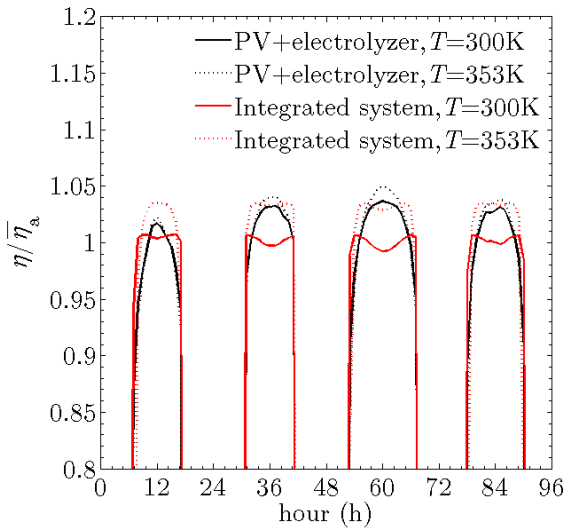

c)

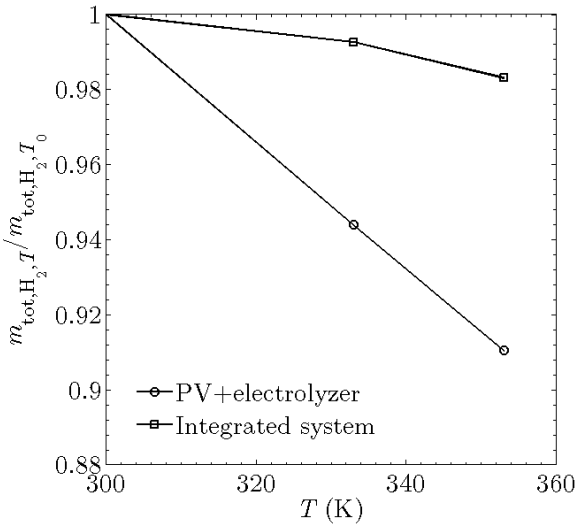

Figure S8. (a) η of a conventional stand-alone PV system with its optimal band-gap combination for the dual absorber tandem-cell (1.0/1.6 eV at all temperatures), electrically connected to a stand-alone electrolyzer, for four typical seasonal days at three isothermal conditions (T = 300, 333, 353 K), and (b) the instantaneous efficiency normalized by $\overline{\eta}_a$ for the stand-alone PV plus stand-alone electrolyzer system compared to the instantaneous efficiency of an integrated solar fuels generator system with l_{el} = 10 mm, t_e = 10 mm, and η_{pc} = 1, at its optimal band-gap combination (0.8/1.6 eV at all temperatures) and (c) the normalized annually integrated fuel production for the conventional system and for the integrated system with m_{tot,H_2,T_0} = 14.0, and 17.4 kg m^{-2} year^{-1} for the PV+electrolyze and integrated system, respectively.

References

1 H. E. Darling, *Journal of Chemical & Engineering Data*, 1964, **9**, 421–426.

2 Y. Sone, P. Ekdunge and D. Simonsson, *Journal of The Electrochemical Society*, 1996, **143**, 1254–1259.

3 J. O. M. Bockris, I. A. Ammar and A. K. M. S. Huq, *The Journal of Physical Chemistry*, 1957, **61**, 879–886.

4 G. Lodi, E. Sivieri, A. Battisti and S. Trasatti, *Journal of Applied Electrochemistry*, 1978, **8**, 135–143.

5 K. Kinoshita, *Electrochemical Oxygen Technology*, John Wiley and Sons, Inc.,, 1992.

6 L. Kriksunov, L. Bunakova, S. Zabusova and L. Krishtalik, *Electrochimica Acta*, 1994, **39**, 137 – 142.

7 N. M. Markovic, B. N. Grgur and P. N. Ross, *The Journal of Physical Chemistry B*, 1997, **101**, 5405–5413.

8 W. Sheng, H. A. Gasteiger and Y. Shao-Horn, *Journal of The Electrochemical Society*, 2010, **157**, B1529–B1536.

9 J. George and C. Menon, *Surface and Coatings Technology*, 2000, **132**, 45 – 48.

10 Y. Varshni, *Physica*, 1967, **34**, 149 – 154.

11 R. Pässler, *physica status solidi (b)*, 2003, **236**, 710–728.

12 P. Singh and N. Ravindra, *Solar Energy Materials and Solar Cells*, 2012, **101**, 36 – 45.

13 A. Damjanovic, A. Dey and J. O. Bockris, *Journal of The Electrochemical Society*, 1966, **113**, 739–746.

14 H. Ito, T. Maeda, A. Nakano and H. Takenaka, *International Journal of Hydrogen Energy*, 2011, **36**, 10527 – 10540.

15 W. Haynes, *CRC Handbook of Chemistry and Physics*, Taylor & Francis, 2011.

16 M. A. Green, K. Emery, Y. Hishikawa, W. Warta and E. D. Dunlop, *Progress in Photovoltaics: Research and Applications*, 2013, **21**, 1–11.